

PICOSECOND PUMP/PROBE ABSORPTION SPECTROSCOPY FOR QUANTITATIVE CONCENTRATION MEASUREMENTS IN TURBULENT, HIGH-PRESSURE FLAMES

Gregory J. Fiechtner,[†]
Galen B. King, and Normand M. Laurendeau
Flame Diagnostics Laboratory
School of Mechanical Engineering
Purdue University
West Lafayette, IN 47907

Abstract--Measurement of flame radical concentrations is important to the understanding of the chemical kinetics involved in combustion. Application of optical techniques allows for non-intrusive determination of the radical concentration. One of the most challenging problems for investigators is obtaining data in high-pressure flames that is independent of the collisional environment. An added complication is turbulence, which requires that data be taken in less than one millisecond. We seek to obviate these difficulties using picosecond pump/probe absorption spectroscopy. This paper is divided into two sections: Part 1 contains the theory used in developing our instrument, and Part 2 contains our most recent measurements.

In Part 1, a picosecond pump/probe absorption model is developed using a rate-equation analysis. Implications are discussed for a laser pulsewidth that is much smaller than the excited-state lifetime of the absorbing atom. The possibility for quantitative, quenching-independent concentration measurements is discussed, and detection limits are estimated. For a three-level model, this development has led to a technique with which the ASOPS instrument can be used to obtain both the electronic quenching rate coefficient and the doublet mixing rate coefficient during a single measurement. The technique, called the dual-beam ASOPS method, is successfully used to measure subnanosecond lifetimes of the $3P$ level of atomic sodium, as discussed in Part 2.

In Part 2, the development and evaluation of our picosecond pump/probe instrument is presented. The asynchronous optical sampling (ASOPS) method is chosen, in which beams from two independent actively mode-locked lasers are crossed in the flame. Verification of the method is obtained through concentration measurements of atomic sodium in an atmospheric methane-air flame. For the first time, ASOPS measurements are made on a quantitative basis. This is accomplished by calibration of the Na concentration using atomic absorption spectroscopy. ASOPS measurements are taken at a rate of 155.7 kHz with only 128 averages, resulting in a corresponding detection limit of $5 \times 10^9 \text{ cm}^{-3}$. The quenching rate coefficient is obtained in a single measurement using the dual-beam ASOPS technique. The magnitude is in excellent agreement with literature values for the present flame conditions. Using the picosecond pump/probe absorption model of Part 1, a detection limit of $2 \times 10^{17} \text{ cm}^{-3}$ is predicted for the $Q_1(9)$ line of $A^2\Sigma^+(v'=0) \leftrightarrow X^2\Pi(v''=0)$ OH at 2000 K. Although this value is too large for practical flame studies, a number of improvements are suggested that will substantially improve the ASOPS detection limit.

[†]Present Address: Center for Combustion Research, Department of Mechanical Engineering, University of Colorado Boulder, CO 80309-0427. E-mail: fiechtne@spot.Colorado.edu

PART 1:

A Picosecond Pump/Probe Absorption Model for Quantitative Concentration Measurements within the Temporal Scale of Turbulent Flames

I. Introduction

Optical methods of measuring species concentrations have provided new insights into the combustion process.¹ The most widely used of these techniques is laser-induced fluorescence (LIF),² because its favorable signal-to-noise ratio (SNR) allows detection of minor species such as the hydroxyl radical. In high-pressure flames under conditions of turbulence, fluctuations in the collisional environment can cause uncertainty in the LIF signal.³ To overcome this difficulty, we have previously examined the possibility of using synchronously mode-locked dye lasers with picosecond pulses in the pump/probe configuration. In particular, the asynchronous optical sampling (ASOPS) technique has been applied to atomic sodium in laminar flames at atmospheric pressure.³

In this paper, we present a model that allows quantitative concentration measurements using picosecond pump/probe absorption spectroscopy. The model is based on the standard rate equations for a small laser irradiance. Using the detection limit for atomic lithium reported by Jones and coworkers,⁴ we predict detection limits for important diatomic flame species such as OH. The model is extended to measurements of excited-state lifetimes, resulting in a novel procedure for obtaining electronic quenching rate coefficients for a multi-level absorber/emitter. We then consider the potential application of high repetition rate, picosecond-pulse laser technology to measurement of concentrations of flame radicals in turbulent reacting flows. Qualitative experimental results for atomic sodium are presented in Part 2, which also summarizes the significant features of the ASOPS method.⁵

II. Assumptions

Before presenting the model, we first discuss some underlying assumptions. First, the laser irradiance is assumed to be small, so that the effects of optical saturation can be ignored. Thus, the present technique should not be confused with the technique of saturated absorption spectroscopy.¹ In fact, the present model is applied here to predict the saturation limit, so that it can purposely be avoided in experiments. Second, optically-thin conditions are assumed, although the present analysis allows the onset of optically-thick conditions to be estimated, so that it can be avoided. Third, all atoms or molecules are assumed to be in the electronic ground state in the absence of laser radiation, i.e., thermal excitation is ignored. Fourth, the spectral bandwidth of a synchronously mode-locked dye laser can be assumed to be significantly larger than that of the absorbing molecules. This allows certain simplifications to be applied when carrying out spectral integrations. Fifth, the spatial profile of the laser is assumed to be uniform. Although this is clearly not true, the interested reader is directed to previous studies that assess the importance of the spatial profile.^{4,6} Sixth, to simplify temporal integration of the excitation dynamics, the temporal laser profile is assumed to be constant, i.e., a top-hat profile. Again, the interested reader is directed to a previous study that analyzes the importance of the temporal laser profile.⁶

Because of limitations associated with our laser systems, our experiments have focused on the detection of atomic sodium.⁵ For this reason, atomic sodium is the subject of most of the calculations in this paper. We have previously shown that stepwise photoionization can be ignored for atomic sodium.³ Although the laser pulsewidth is much smaller than the excited-state lifetime of atomic sodium, we also ignore the possibility of coherent transient phenomena. As discussed by Altkorn and Zare,⁷ coherent effects can be ignored if the coherence time of the laser is short compared to the reciprocal of the absorption or stimulated emission probability. Using the present model, this limit can be avoided. Indeed, most of our results are free from any such effects.⁵ This allows us to apply rate equation theory to model the pump/probe absorption process.

III. Rate Equation Method

As an introduction to the modelling process, we first consider the two-level absorber/emitter of Fig. 1(a). The pump laser is tuned to resonance with the $1 \rightarrow 2$ transition, while the probe laser is tuned to resonance with either the $1 \rightarrow 2$ or the $2 \rightarrow 3$ transition. However, in many cases it is necessary to include an additional intermediate level; for example, our measurements require two intermediate states to adequately model the

$3P_{1/2,3/2}$ doublet of atomic sodium.⁵ To demonstrate the difficulties that can arise in this situation, we also consider the three-level absorber/emitter of Fig. 1(b). Here, the pump laser can be tuned to either the $1 \rightarrow 2$ or the $1 \rightarrow 3$ transitions, while the probe laser can be tuned to either the $1 \rightarrow 2$, $1 \rightarrow 3$, $2 \rightarrow 4$, or $3 \rightarrow 4$ transitions. In Fig. 1, the number density of the i^{th} level is denoted by N_i (cm^{-3}), while the total number density, N_T (cm^{-3}), is the sum of the number densities over all the levels of a particular model.

We now define a number of processes associated with the models of Fig. 1. The laser interacts with the absorber/emitter through W_{ij} and W_{ji} , which represent the rate coefficients for stimulated absorption and stimulated emission (s^{-1}) between levels i and j , respectively. The Einstein rate coefficient for spontaneous emission is denoted by A_{ji} (s^{-1}). Population transfer is also allowed to take place as a result of collisional transfer. Thus, Q_{ji} represents the collisional de-excitation rate coefficient, often called the quenching rate coefficient (s^{-1}). Because the transitions in question occur in the visible or ultraviolet regions of the spectrum, collisional excitation is negligible relative to quenching.³ For the same reason, the excited-state population is negligible in the absence of laser radiation, so that $N_T \approx N_1$. In Fig. 1(b), Q_{23} and Q_{32} represent the mixing rate coefficients between levels 2 and 3.

We now derive suitable expressions for the pump/probe absorption signal. First, the excitation that is caused by the pump laser will be considered. The resulting absorption of pump-beam photons will then be modelled. Finally, the ensuing perturbation of the probe-beam irradiance will be analyzed.

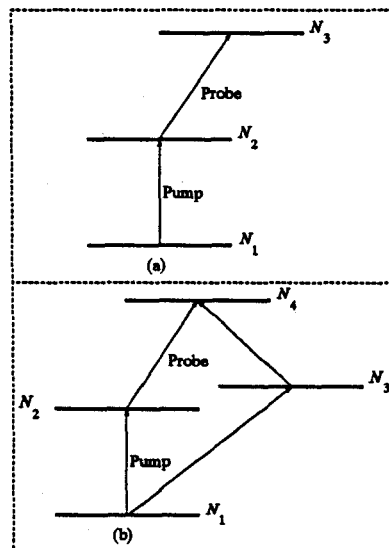


Fig. 1 Pump/probe diagrams corresponding to (a) a two-level absorber/emitter and (b) a three-level absorber/emitter. In both cases, one level is added to account for the probe, resulting in a total of three and four levels, respectively.

IV. Excitation Process

The population of excited atoms will be determined by the pump irradiance, temporal width, and bandwidth. The atomic population density and bandwidth are equally important considerations. In this section, we model the excitation process for a synchronously mode-locked dye laser as the external light source. Expressions will be developed for both the linear and the saturated limits. From these expressions, a "saturation parameter"⁶ will be defined, so that saturation can be avoided in the subsequent experiments.⁵ Close attention will be paid to the effects of extremely short, mode-locked pulsewidths. For ultrashort pulses, we show that the steady-state rate equations are not valid, and that saturation will not take place until the laser irradiance is much greater than that predicted by a steady-state analysis. During the presence of an ultrashort pulse, the rate equations for a three-level absorber/emitter are found to reduce to those for a two-level model in terms of the resonantly-coupled levels.

A. Two-Level Model

The excited-state number density can be related to the total number density by writing the rate equation for a two-level atom:²

$$\frac{dN_2(z,t)}{dt} = N_1(z,t)W_{12} - N_2(z,t)(W_{21} + Q_{21} + A_{21}), \quad (1)$$

where $Q_{12} \gg Q_{12}$.⁸ The stimulated Einstein rate coefficients can be written as⁹

$$W_{12}(z,t) = \frac{g_2}{g_1} W_{21}(z,t) = \frac{B_{12}}{c} \int_{-\infty}^{\infty} I_{\nu}^L(z,t) Y(\nu) d\nu, \quad (2)$$

where $I_{\nu}^L(z,t)$ is the laser spectral irradiance in the z -direction. The quantities g_i represent the degeneracy of the i^{th} state. By applying the appropriate spectral and temporal approximations, W_{12} can be expressed in terms of the average laser power, as shown in Section V.

Noting that $N_1 + N_2 = N_T$, the rate equation for level 2 becomes

$$\frac{dN_2(z,t)}{dt} = N_T(z,t)W_{12} - N_2(z,t) \left[\left(1 + \frac{g_1}{g_2}\right) W_{12} + T_{21} \right], \quad (3)$$

where $T_{ji} = Q_{ji} + A_{ji}$. The functional dependence of the population density on position z and time t will not be retained below, thereby reducing cumbersome notation.

i. Steady-State Solution

A number of situations arise in which the time-dependent nature of Eq. (3) can be ignored. At steady-state, $dN_2/dt = 0$, and Eq. (3) yields

$$(N_2)_{ss} = \frac{N_T W_{12}}{\left(1 + \frac{g_1}{g_2}\right) W_{12} + T_{21}}. \quad (4)$$

Equation (4) will apply for (1) cw laser excitation or (2) at the peak of a laser pulse with temporal width that is sufficiently large compared to the lifetime of level 2.² Two practical limits of Eq. (4) result for extremely small or large incident laser irradiance. For small laser irradiance, $W_{12} \ll T_{21}$, and Eq. (4) reduces to

$$(N_2)_{ss}^{LIN} = \frac{N_T W_{12}}{T_{21}}. \quad (5)$$

As the laser spectral irradiance is increased to extremely large values, $W_{12} \gg T_{21}$, and

$$(N_2)_{ss}^{SAT} = \left(\frac{g_2}{g_1 + g_2} \right) N_T. \quad (6)$$

ii. Time-Dependent Solution

Define the upward and downward rate coefficients as

$$R_{12} = W_{12}, \quad (7a)$$

and

$$R_{21} = W_{21} + T_{21}, \quad (7b)$$

respectively. Equation (1) can then be written

$$\frac{dN_2^*}{dt} = N_1^* R_{12} - N_2^* R_{21}, \quad (8)$$

where the dimensionless population densities have been defined as

$$N_i^* = \frac{N_i}{N_T}. \quad (9)$$

Assuming a top-hat temporal laser pulse, Eq. (8) becomes

$$N_2^* = \frac{(N_2)_{ss}}{N_T} \{1 - \exp[-(R_{12} + R_{21})t]\} + N_2^* \exp[-(R_{12} + R_{21})t]. \quad (10)$$

B. Three-Level Model

Models for sodium and other alkalis require an additional level because of spectroscopic doublets. Here, level 1 is again the ground level, while levels 2 and 3 are reserved for the doublet levels. The first-order exponential term of Eq. (10) will no longer apply since two first-order rate equations must be solved simultaneously. Due to the presence of the additional level, the following rate coefficients must be introduced:

$$R_{13} = W_{13}, \quad (11a)$$

and

$$R_{31} = W_{31} + T_{31}, \quad (11b)$$

along with the doublet mixing rate coefficients, Q_{23} and Q_{32} . To further reduce the cumbersome notation, we also introduce the following rate coefficients:

$$R_a = R_{12} + R_{21} + Q_{23}, \quad (12a)$$

$$R_b = R_{13} + R_{31} + Q_{32}, \quad (12b)$$

$$R_c = Q_{32} - R_{12}, \quad (12c)$$

and

$$R_d = Q_{23} - R_{13}. \quad (12d)$$

Noting that $N_1 = N_T - (N_2 + N_3)$, the rate equations for levels 2 and 3 can be expressed as

$$\frac{dN_2}{dt} = -R_a N_2 + R_c N_3 + R_{12} N_T, \quad (13a)$$

and

$$\frac{dN_3}{dt} = -R_b N_3 - R_d N_2 + R_{13} N_T. \quad (13b)$$

i. Steady-State Solution

The steady-state, three-level solution has been extensively reported in the literature.² The solution is given here because of its importance to later discussions, for which clarification of our nomenclature will be necessary.

Applying the steady-state assumption, and simultaneously solving the resulting linear algebraic equations, we obtain

$$(N_2)_{ss} = \frac{R_{12} R_b + R_{13} R_c}{R_a R_b - R_c R_d} N_T, \quad (14a)$$

and

$$(N_3)_{ss} = \frac{R_{12} R_d + R_{13} R_a}{R_a R_b - R_c R_d} N_T. \quad (14b)$$

For exclusive excitation of level 2, $W_{13} = W_{31} = 0$, so that

$$(N_2^{(2)})_{ss} = \frac{W_{12}(T_{31} + Q_{32})N_T}{W_{12}(T_{31} + Q_{23} + Q_{32}) + W_{21}(T_{31} + Q_{32}) + T_{21}(T_{31} + Q_{32}) + Q_{23}T_{31}}, \quad (15a)$$

and

$$(N_3^{(2)})_{ss} = \frac{W_{12}Q_{23}N_T}{W_{12}(T_{31} + Q_{23} + Q_{32}) + W_{21}(T_{31} + Q_{32}) + T_{21}(T_{31} + Q_{32}) + Q_{23}T_{31}}. \quad (15b)$$

For small laser irradiance, $W_{12} \ll Q_{ij}$, and thus

$$(N_2^{(2)})_{ss}^{LIN} = \frac{W_{12}(T_{31} + Q_{32})N_T}{T_{21}(T_{31} + Q_{32}) + Q_{23}T_{31}}, \quad (16a)$$

and

$$(N_3^{(2)})_{ss}^{LIN} = \frac{W_{12}Q_{23}N_T}{T_{21}(T_{31} + Q_{32}) + Q_{23}T_{31}}. \quad (16b)$$

In the limit of infinite laser irradiance, Eqs. (15a) and (15b) become

$$(N_2^{(2)})_{ss}^{SAT} = \left[\frac{T_{31} + Q_{32} + Q_{23}}{T_{31} + Q_{32}} + \frac{g_1}{g_2} \right]^{-1} N_T, \quad (17a)$$

and

$$(N_3^{(2)})_{ss}^{SAT} = \left[\frac{T_{31} + Q_{32} + Q_{23}}{Q_{23}} + \left(\frac{g_1}{g_2} \right) \frac{T_{31} + Q_{32}}{Q_{23}} \right]^{-1} N_T. \quad (17b)$$

Now, for the exclusive excitation of level 3, $W_{12} = W_{21} = 0$, so that

$$(N_2^{(3)})_{ss} = \frac{W_{13}Q_{32}N_T}{W_{13}(T_{21} + Q_{23} + Q_{32}) + W_{31}(T_{21} + Q_{23}) + T_{21}(T_{31} + Q_{32}) + Q_{23}T_{31}}, \quad (18a)$$

and

$$(N_3^{(3)})_{ss} = \frac{W_{13}(T_{21} + Q_{23})N_T}{W_{13}(T_{21} + Q_{23} + Q_{32}) + W_{31}(T_{21} + Q_{23}) + T_{21}(T_{31} + Q_{32}) + Q_{23}T_{31}}. \quad (18b)$$

For small laser irradiance, $W_{13} \ll Q_{ij}$, and thus

$$(N_2^{(0)})_{ss}^{LIN} = \frac{W_{12}Q_{32}N_T}{T_{21}(T_{31}+Q_{32})+Q_{23}T_{31}}, \quad (19a)$$

and

$$(N_3^{(0)})_{ss}^{LIN} = \frac{W_{13}(T_{21}+Q_{23})N_T}{T_{21}(T_{31}+Q_{32})+Q_{23}T_{31}}. \quad (19b)$$

In the limit of infinite laser irradiance, we obtain

$$(N_2^{(0)})_{ss}^{SAT} = \left[\frac{T_{21}+Q_{23}+Q_{32}}{Q_{32}} + \left(\frac{g_1}{g_3} \right) \frac{T_{21}+Q_{23}}{Q_{32}} \right]^{-1} N_T, \quad (20a)$$

and

$$(N_3^{(0)})_{ss}^{SAT} = \left[\frac{T_{21}+Q_{23}+Q_{32}}{T_{21}+Q_{23}} + \frac{g_1}{g_3} \right]^{-1} N_T. \quad (20b)$$

ii. Time-Dependent Solution

The transient solution of the three-level rate equations has been extensively reported by, for example, Hercher,¹⁰ Measures,¹¹ Olivares and Hieftje,¹² Boutilier *et al.*,¹³ Zizak *et al.*,¹⁴ Omenetto *et al.*,¹⁵ Cattolica *et al.*,¹⁶ Alkemade,⁶ Omenetto *et al.*,¹⁷ and Axner *et al.*¹⁸ The results are now summarized, so that the appropriate expressions can be used in the pump/probe model.

Introducing the dimensionless population densities from Eq. (9), Eqs. (13) can be written

$$\frac{dN_2^*}{dt} = -R_d N_2^* + R_c N_3^* + R_{12}, \quad (21a)$$

and

$$\frac{dN_3^*}{dt} = R_d N_2^* - R_c N_3^* + R_{13}. \quad (21b)$$

These equations can be solved to yield the eigenvalues¹⁹

$$r_1 = \frac{1}{2} \left(-(R_a + R_b) + \sqrt{(R_a + R_b)^2 - 4(R_a R_b - R_c R_d)} \right), \quad (22a)$$

and

$$r_2 = \frac{1}{2} \left(-(R_a + R_b) - \sqrt{(R_a + R_b)^2 - 4(R_a R_b - R_c R_d)} \right). \quad (22b)$$

The resulting solution can be shown to take the form¹⁹

$$N_2^* = \left[\frac{-R_{12}(R_a + r_2) + R_{13}R_c}{r_1(r_1 - r_2)} + C_1 \right] e^{r_1 t} + \left[\frac{R_{12}(R_a + r_1) - R_{13}R_c}{r_2(r_1 - r_2)} + C_2 \right] e^{r_2 t} + \frac{-R_{12}(R_a + r_1 + r_2) + R_{13}R_c}{r_1 r_2}, \quad (23a)$$

and

$$N_3^* = \frac{(R_a + r_1)}{R_c} \left[\frac{-R_{12}(R_a + r_2) + R_{13}R_c}{r_1(r_1 - r_2)} + C_1 \right] e^{r_1 t} + \frac{(R_a + r_2)}{R_c} \left[\frac{R_{12}(R_a + r_1) - R_{13}R_c}{r_2(r_1 - r_2)} + C_2 \right] e^{r_2 t} + \frac{-R_{12}(R_a + r_1)(R_a + r_2) + R_{13}R_c R_c}{r_1 r_2 R_c}. \quad (23b)$$

Evaluating the constants C_1 and C_2 at time $t=0$,

$$C_1 = \frac{-R_c N_{3,0}^* + (R_a + r_2) N_{2,0}^*}{(r_2 - r_1)}, \quad (24a)$$

and

$$C_2 = \frac{R_c N_{3,0}^* - (R_a + r_1) N_{2,0}^*}{(r_2 - r_1)}, \quad (24b)$$

where $N_{2,0}^*$ and $N_{3,0}^*$ are the initial dimensionless excited-state population densities, which vanish for negligible thermal excitation in the absence of laser radiation.

At this point, writing out the solution in terms of the original rate coefficients would be an algebraic nightmare. Rather, consider the application of these results to atomic sodium. In particular, we wish to model the non-equilibrium population density distributions of the sodium D lines in the absence of external radiation, for which $W_{12} = W_{21} = W_{31} = W_{13} = 0$. Let 1, 2, and 3 denote the $3S_{1/2}$, $3P_{1/2}$, and $3P_{3/2}$ states, respectively. Since only 0.6 nm separates the D_1 and D_2 transitions, we may assume that $Q_{21} = Q_{31} = Q$. In addition, for sodium $A_{21} \approx A_{31} \approx A$. Under these assumptions, $R_{12} = R_{13} = 0$, $R_{21} = R_{31} = Q + A$, $R_a = Q + A + Q_{23}$, $R_b = Q + A + Q_{32}$, $R_c = Q_{32}$, $R_d = Q_{23}$, $r_1 = -Q - A$, and $r_2 = -Q - A - Q_{23} - Q_{32}$.

The resulting expressions for the dimensionless population densities reduce to

$$N_2^*(t) = \frac{Q_{32}}{Q_{23} + Q_{32}} \{ (N_{3,0}^* + N_{2,0}^*) \exp[-(Q + A)t] - \left(N_{3,0}^* - \frac{Q_{23}}{Q_{32}} N_{2,0}^* \right) \exp[-(Q + A + Q_{23} + Q_{32})t] \}, \quad (25a)$$

and

$$N_3^*(t) = \frac{Q_{23}}{Q_{23} + Q_{32}} \{ (N_{3,0}^* + N_{2,0}^*) \exp[-(Q + A)t] + \left(\frac{Q_{32}}{Q_{23}} N_{3,0}^* - N_{2,0}^* \right) \exp[-(Q + A + Q_{23} + Q_{32})t] \}. \quad (25b)$$

For $N_{3,0}^* = 0$, these relationships are identical to those presented by

Takubo *et al.*²⁰ By relating levels 2 and 3 via the principle of detailed balancing, we can show that $Q_{23} = 2Q_{32}$ at flame temperatures.²¹ The dimensionless number densities of the excited doublets are then

$$N_2^*(t) = \frac{1}{3} \{ (N_{3,0}^* + N_{2,0}^*) \exp[-(Q + A)t] - (N_{3,0}^* - 2N_{2,0}^*) \exp[-(Q + A + 3Q_{32})t] \}, \quad (26a)$$

and

$$N_3^*(t) = \frac{2}{3} \left\{ (N_{3,0}^* + N_{2,0}^*) \exp[-(Q + A)t] + \left(\frac{1}{2} N_{3,0}^* - N_{2,0}^* \right) \exp[-(Q + A + 3Q_{32})t] \right\}. \quad (26b)$$

These expressions will be used in Section IX to develop a model for common temporal pump/probe results, such as those obtained when using the ASOPS instrument for atomic sodium.⁵

V. Characteristics of Synchronously Mode-Locked Laser Radiation

Before continuing with the present rate equation analysis, we must express the stimulated absorption rate coefficient, W_{12} , in terms of practical experimental parameters. The evaluation of W_{12} requires the application of both spectral and temporal approximations concerning the output of a synchronously mode-locked dye laser.

A. Spectral Approximations

Absorption theory requires knowledge of the laser spectral lineshape, and in particular, its bandwidth (FWHM), $\Delta\nu_{1/2}^L$ (s^{-1}). For a synchronously mode-locked dye laser, the spectral bandwidth can be estimated from the laser pulsewidth, which can easily be measured using second-harmonic autocorrelation. The spectral lineshape is related to the autocorrelation pulseshape because the output pulses are nearly Fourier-transform limited.²² In this case, $\Delta\nu_{1/2}^L \Delta t_{1/2}^L$ is a constant, where $\Delta t_{1/2}^L$ (s) is the temporal pulsewidth (FWHM).

When the output pulses are nearly transform-limited, the time-bandwidth product depends on the shape of the distribution function for the spectral and temporal pulseshapes. For example, a sech^2 pulseshape results in a time-bandwidth product of 0.32, while a truncated exponential pulseshape results in a corresponding value of 0.11.²²⁻²⁴ Blanchard and Wirth²⁴ have shown that the spectral distribution of a pulse is best-modelled using a sech^2 function, although the agreement is not perfect. Choosing this function, the spectral lineshape function of the laser can be written¹⁹

$$Y^L(\nu) = \frac{\ln\left(\frac{1}{\sqrt{2}-1}\right)}{\Delta\nu_{1/2}^L} \text{sech}^2 \left[\frac{2\ln\left(\frac{1}{\sqrt{2}-1}\right)}{\Delta\nu_{1/2}^L} (\nu - \nu_0^L) \right]. \quad (27)$$

The rate equations are usually expressed in terms of the absorption rate coefficient W_{12} , which is given by the integral of Eq. (2). A typical pulsewidth for our laser systems is 20 psec,⁵ for which the time-bandwidth product yields the value $\Delta\nu_{1/2}^L = 1.58 \times 10^{10} s^{-1}$. This is much larger than the sodium linewidth of $\Delta\nu_{1/2} = 2.7 \times 10^9 s^{-1}$,⁵ so that $\Delta\nu_{1/2}^L \gg \Delta\nu_{1/2}$. In this case, Eq. (2) can be evaluated by holding the laser spectral irradiance constant at its centerline value, and removing it from the integral.^{9,25} Hence, the stimulated rate coefficient and the laser irradiance are related by¹⁹

$$W_{12} = \frac{B_{12} \ln\left(\frac{1}{\sqrt{2}-1}\right)}{c \Delta\nu_{1/2}^L} I^L = \frac{g_2 A_{21} c^2 \ln\left(\frac{1}{\sqrt{2}-1}\right)}{g_1 8\pi h\nu_0^L \Delta\nu_{1/2}^L} I^L. \quad (28)$$

where I^L is the total laser irradiance.

B. Temporal Approximations

From an experimental standpoint, the total laser irradiance is not a practical quantity, since average power is usually measured. Depending on the temporal laser pulse shape, the relationship between average power and irradiance may be complicated. To simplify the mathematical modelling of the interaction of laser radiation with an atomic species, each mode-locked laser pulse can be temporally modelled as a top-hat profile. In this case, we obtain the expressions¹⁹

$$W_{12} = \frac{g_2}{g_1} \frac{c^2 A_{21} \ln\left(\frac{1}{\sqrt{2}-1}\right) P_{\text{Avg}}^L}{2\pi^2 D^2 \ln^2 \Delta\nu_{1/2}^L \Delta t_{1/2}^L f^L}, \quad (29)$$

where P_{Avg}^L is the average laser power (W), D is the focal diameter when assuming a cylindrical beam (cm^2), and f^L is the laser repetition frequency (Hz). For our lasers, f^L is approximately 82 MHz.⁵ In addition, the geometry of Fig. 2 has been applied, where $dV = A_c dz$, and $A_c = \pi D^2/4$ is the cross-sectional area of the beam (cm^2). The laser irradiance can be expressed in terms of the energy per pulse (J), E_p^L , by the relation¹⁹

$$E_p^L = A_c \Delta t_{1/2}^L f^L, \quad (30a)$$

which can, in turn, be substituted into Eq. (28) to obtain

$$W_{12} = \frac{g_2}{g_1} \frac{c^2 A_{21} \ln\left(\frac{1}{\sqrt{2}-1}\right) E_p^L}{2\pi^2 D^2 \ln^2 \Delta\nu_{1/2}^L \Delta t_{1/2}^L}. \quad (30b)$$

These laser-specific equations are now used in the present analysis to calculate practical operating limits for a picosecond pump/probe absorption instrument.

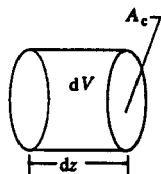


Fig. 2 Differential interaction volume.

VI. Short Pulsewidth Approximations

The ASOPS experiments for which this model has been developed will require knowledge of the extent of the linear range. A good estimate of the onset of saturation is the saturation parameter, which is defined as the laser irradiance for which the linear and saturated limits intersect.⁶ For the steady state two-level model, the stimulated absorption rate at saturation is obtained by intersecting Eq. (5) with Eq. (6) and solving for W_{12} , yielding the expression

$$(W_{12})_{ss}^{\text{SAT}} = \frac{T_{21} g_2}{g_1 + g_2}. \quad (31)$$

For the sodium values of Table I, the resulting steady-state saturation parameter becomes $(W_{12})_{ss}^{\text{SAT}} = 1.3 \times 10^9 \text{ s}^{-1}$, which corresponds from Eq. (29) to an average laser power of only $(P_{\text{Avg}}^L)_{ss}^{\text{SAT}} = 34 \mu\text{W}$. For the latter calculation, the laser-specific values of Table II were applied. These values are used for all relevant calculations throughout this paper, unless otherwise noted.

Table I Spectroscopic quantities utilized in several of the calculations in this paper. The spectroscopic quantities are for the D_2 line of atomic sodium.¹⁸

Transition	$3S_{1/2} \rightarrow 3P_{3/2}$
ν_0	$5.0934 \times 10^{14} \text{ s}^{-1}$
g_2	4
g_1	2
A_{21}	$6.15 \times 10^7 \text{ s}^{-1}$

Table II Quantities utilized in several of the calculations in this paper. The laser parameters are for a synchronously mode-locked dye laser, for which the time-bandwidth product is assumed to be 0.315.²³ The geometrical quantities correspond to the focal volume we have chosen to model. Collisional quantities are obtained from literature values for atomic sodium in an atmospheric hydrocarbon flame.³

Notation for Q_{ij}	Levels 1, 2, and 3 are $3S_{1/2}$, $3P_{1/2}$ and $3P_{3/2}$
$Q_{21} = Q_{31}$	$2 \times 10^9 \text{ s}^{-1}$
Q_{32}	$4 \times 10^9 \text{ s}^{-1}$
$(\Delta\nu_{1/2})_c$	$2.7 \times 10^9 \text{ s}^{-1}$
$\Delta t_{1/2}^L$	$20 \times 10^{-12} \text{ s}$ (unless stated otherwise)
$\Delta\nu_{1/2}^L$	$1.58 \times 10^{10} \text{ s}^{-1}$
f^L	$82 \times 10^6 \text{ s}^{-1}$
D	$7.6 \times 10^{-3} \text{ cm}$
Crossing Angle	2.9°

The values of Table I are compiled under the assumption that sodium is a two-level absorber. These values correspond to the $3S_{1/2} \rightarrow 3P_{3/2}$ transition, which is denoted as the 1→2 transition. Unfortunately, we also must treat sodium as a three-level absorber in many of our calculations. For this reason, Table III is also included in this paper. The convention for Table III is that the $3S_{1/2}$, $3P_{1/2}$ and $3P_{3/2}$ levels are denoted by levels 1, 2 and 3, respectively. In the case of the three-level model with direct excitation of level 3, the saturation parameter is obtained by intersecting Eq. (19b) with Eq. (20b), and solving for W_{13} . The resulting saturation parameter becomes

$$(W_{13})_{ss}^{\text{SAT}} = \frac{T_{21}(T_{31} + Q_{32}) + Q_{23}T_{31}}{T_{21} + Q_{23} + Q_{32} + \frac{g_1}{g_3}(T_{21} + Q_{23})}. \quad (32)$$

Substituting values from Tables II and III, the saturation parameter is $(W_{13})_{ss}^{\text{SAT}} = 1.5 \times 10^9 \text{ s}^{-1}$ which corresponds to a saturation power of only $40 \mu\text{W}$.

Previous experiments concerning the onset of saturation with mode-locked lasers for atomic sodium in atmospheric-pressure flames resulted in a much higher value of the saturation parameter.^{3,26} This discrepancy arises, in part, because true steady-state conditions are not achieved for the small $\Delta t_{1/2}^L$ values of mode-locked pulses. To illustrate this effect, we rearrange Eq. (3) in the form

$$\tau_r \frac{dN_2}{dt} + N_2 = N_T W_{12} \tau_r, \quad (33a)$$

from which it is clear that the time-constant of the two-level system is given by²⁷

$$\tau_r = \left[\left(1 + \frac{g_1}{g_2} \right) W_{12} + T_{21} \right]^{-1}. \quad (33b)$$

Omenetto *et al.*^{15,28} refer to this quantity as the "response time" of the system. For pulsewidths small compared to this quantity, the steady-state assumption will yield a large dynamic error.

Table III Spectroscopic and laser quantities utilized in many of the calculations throughout this paper. The spectroscopic quantities are for the D -lines of atomic sodium.¹⁸ Levels 1, 2, and 3 denote the $3S_{1/2}$, $3P_{1/2}$ and $3P_{3/2}$ levels, respectively.

g_2	2
g_3	4
g_1	2
A_{21}	$6.13 \times 10^7 \text{ s}^{-1}$
A_{31}	$6.15 \times 10^7 \text{ s}^{-1}$
ν_{13}	$5.0934 \times 10^{14} \text{ s}^{-1}$
ν_{12}	$5.0883 \times 10^{14} \text{ s}^{-1}$

A. Two-Level Model

For a two-level model, the steady-state equation should be replaced by^{6,13}

$$N_2 = (N_2)_{ss} [1 - \exp(-(W_{12} + W_{21} + T_{21})\Delta t_{1/2}^L)] \quad (34)$$

For $W_{12} \ll T_{21}$, we may expand the exponential assuming small $\Delta t_{1/2}^L$ and employ Eq. (5) to obtain²⁹

$$(N_2)^{LN} = N_2 W_{12} \Delta t_{1/2}^L \quad (35)$$

Thus the increase in excited-state population is directly proportional to both the incident laser power and the pulsewidth. The saturation curve of Eq. (34) is compared with the steady-state curve of Eq. (4) in Fig. 3. The values of Table I were used in calculating these curves. As shown, the steady-state approximation drastically underestimates the saturation parameter for short pulsewidths (7 psec, in this case). The appropriate linear limits from Eqs. (5) and (35) are also shown in Fig. 3. For $W_{12} \gg T_{21}$, the exponential term in Eq. (34) vanishes, and we again obtain Eq. (6). Intersecting this saturation limit with Eq. (35), the saturation parameter for the two-level, short-pulsewidth model becomes

$$(W_{12})^{SAT} = \frac{g_2}{(g_1 + g_2)\Delta t_{1/2}^L} \quad (36)$$

Hence the laser power at which saturation becomes important increases as the laser pulsewidth decreases.^{6,13} Using the values of Table I and Table II, and assuming that $\Delta t_{1/2}^L = 7$ psec, Eq. (36) predicts $(W_{12})^{SAT} = 9.5 \times 10^{10} \text{ s}^{-1}$ or $(P_{AV}^L)^{SAT} = 2.5 \text{ mW}$. This represents a factor of 74 increase in the saturation parameter over that defined by the two-level, steady-state model. In previous experiments, saturation was observed to be delayed until approximately 30–40 mW.³ The additional order-of-magnitude delay probably results from the small irradiance that is present in the spatial and temporal wings of the laser pulse.⁶ This effect has been encountered previously in experiments on laser-saturated fluorescence using pulsed lasers.³⁰ Nevertheless, in our experiments the average laser power is always selected to be less than the predicted saturation parameter.⁵

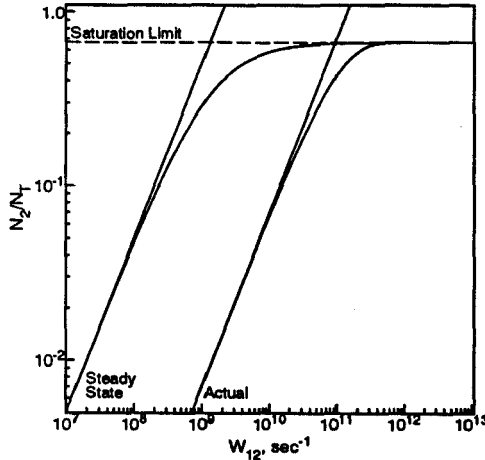


Fig. 3 Saturation curves for a two-level model.^{6,13,15} The left saturation curve is obtained using the values of Tables I and II in the steady-state Eq. (4), and the superimposed linear limit is obtained from Eq. (5). The saturation curve shifted to the right is obtained from Eq. (34) with the superimposed linear limit from Eq. (35). The short-pulsewidth saturation limit is temporally delayed by two orders of magnitude, and the saturation curve has a distorted shape. The pulsewidth used in generating this plot is 7 ps, since the study was originally done in conjunction with a previous experiment.²⁶

B. Three-level Model

The response time of the three-level model is not defined as easily as the two-level case, since a critically-damped, second-order system must now be considered.²⁷ Nevertheless, for $W_{12} = 0$ and negligible thermal excitation, Eq. (23b) can be written in a fashion analogous to the two-level case,^{6,15} i.e.,

$$N_3^{(3)} = (N_3^{(3)})_{ss} \left\{ \frac{r_2(R_a + r_1)}{R_a(r_1 - r_2)} \exp(r_1 \Delta t_{1/2}^L) - \frac{r_1(R_a + r_2)}{R_a(r_1 - r_2)} \exp(r_2 \Delta t_{1/2}^L) + 1 \right\} \quad (37)$$

where $(N_3^{(3)})_{ss}$ is given by Eq. (18b). For small $\Delta t_{1/2}^L$ and W_{13} , the two exponential terms in Eq. (37) can, as above, be approximated linearly, yielding¹⁶

$$(N_3^{(3)})^{LN} = (N_3^{(3)})_{ss}^{LN} \left(\frac{r_1 r_2 \Delta t_{1/2}^L}{R_a} \right) = W_{13} \Delta t_{1/2}^L N_T \quad (38)$$

where we have employed Eq. (19b). The saturation curve generated using Eq. (37) and the values of Table III is plotted in Fig. 4 along with the corresponding steady-state curve from Eq. (18b). Again, the steady-state approximation drastically underpredicts the saturation parameter. Unlike the two-level case, however, the curve of Eq. (37) approaches a saturated population somewhat larger than that of the three-level, steady state model. The reasons for this result will become clear below.

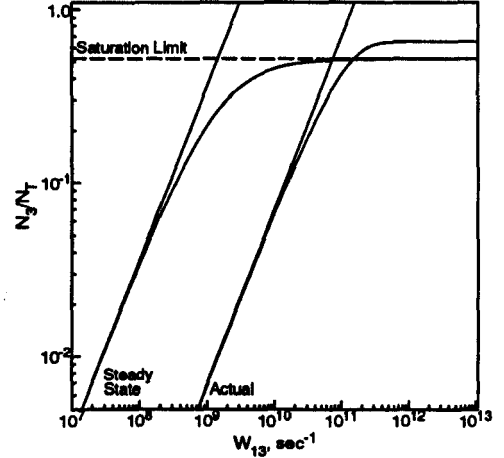


Fig. 4 Saturation curves for a three-level model with direct excitation of level 3 using the values of tables II and III.^{6,13,15} The left saturation curve results from the steady-state Eq. (18b), with the superimposed linear limit, Eq. (19b). The right saturation curve results when correctly accounting for the ultrashort pulse using Eq. (37) with the superimposed linear limit, Eq. (38). The short pulsewidth causes a delay in the onset of saturation, a distortion in the curve shape, and a different saturation limit. The pulsewidth used in generating this plot is 7 ps, since the study was originally done in conjunction with a previous experiment.²⁶

In the case of saturation, the exponential expansion can no longer be made, although $\Delta t_{1/2}^L$ is small, since W_{13} is now extremely large. In this case, the eigenvalues must be expanded and then approximated accordingly.^{11,13} We first write the eigenvalues of Eqs. (22a) and (22b) in the form

$$r_i = -\frac{1}{2}(R_a + R_b) \left\{ 1 \mp \left[1 - \frac{4(R_a R_b - R_c R_d)}{(R_a + R_b)^2} \right]^{1/2} \right\} \quad (39)$$

If the following definition is made,

$$x = \frac{4(R_a R_b - R_c R_d)}{(R_a + R_b)^2} \quad (40)$$

for which the condition $x \ll 1$ corresponds to the condition $W_{13} \gg Q_{ij}$, then the system eigenvalues can be expanded and simplified by ignoring terms of second order and higher, yielding the expressions

$$r_1^{SAT} = -\frac{R_a R_b - R_c R_d}{R_a + R_b} \quad (41)$$

and

$$r_2^{SAT} = -(R_a + R_b) + \frac{R_a R_b - R_c R_d}{R_a + R_b} \quad (41)$$

We now apply these approximations to Eq. (37) and note that r_2^{SAT} varies directly with W_{13} while r_1^{SAT} does not depend on W_{13} . Thus as $W_{13} \rightarrow \infty$, Eq. (37) becomes

$$(N_3^{(3)})^{\text{SAT}} = \frac{W_{12}R_bN_T}{R_aR_b - R_aR_d} \left\{ \left[\frac{R_aR_b - R_aR_d}{R_a(R_a + R_b)} - 1 \right] \exp(r_1\Delta\nu_{1/2}^L) + 1 \right\}. \quad (43)$$

Since r_1^{SAT} is independent of laser power, the small pulsewidths in question will cause the remaining exponential to approach unity, thereby yielding

$$(N_3^{(3)})^{\text{SAT}} = \frac{W_{12}N_T}{R_a + R_b} = \frac{N_T g_3}{g_1 + g_3}. \quad (44)$$

Eqs. (38) and (44) indicate that for mode-locked laser pulses, the rate equations for the three-level model reduce to those corresponding to a short-pulsewidth two-level model for the transition in resonance. This is true for both the linear and saturated regimes, although the linear approximation will hold for comparatively longer pulsewidths. This conclusion is similar to that for which the balanced cross-rate model holds.³¹

VII. Transient Absorption of Picosecond Pulses

An expression that relates the amount of absorbed laser light to a number density is required to interpret experimental results. Based on the previous short-pulsewidth analysis, we can now employ a two-level model. Another important consequence of the transient rate equation analysis is that for short pulses, the excited-state population is independent of quenching. This fact was utilized to obtain quenching-independent concentrations by Stepowski and Cottreau using LIF²⁹, and by Beaman⁴ and Langley *et al.*⁴ using crossed-beam absorption with synchronously mode-locked dye lasers. An unfortunate consequence is that the number of excited atoms is reduced by the factor¹

$$\frac{(N_2)_{\text{SS}}^{\text{LIN}}}{(N_2)^{\text{LIN}}} = \frac{1}{T_{21}\Delta\nu_{1/2}^L}, \quad (45)$$

which for $\Delta\nu_{1/2}^L = 20$ ps and $T_{21} = 1 \times 10^9 \text{ s}^{-1}$ becomes 50.

Since fewer molecules are excited for a given W_{12} by a mode-locked pulse than by a pulse of comparatively-long temporal width, one might expect the absorption to be correspondingly smaller. When calculating the degree of absorption, N_1 and N_2 are normally assumed to be constant with respect to time. However, when exciting with a mode-locked pulse, the excited-state population does not achieve steady state; for a top-hat profile of small irradiance, N_2 will instead increase linearly with time as shown by Eq. (35). Thus a steady-state analysis for estimating the absorbance will be inappropriate, requiring an alternative derivation. To this end, consider again the differential control volume of Fig. 2. Upon passage of a weak pulse through the volume, the resulting excited-state population is given by Eq. (35). Since quenching is negligible on the time scale of a single pulse, and stimulated emission is negligible for low laser irradiance, each excited atom that remains after a mode-locked pulse has traversed the control volume must correspond to the loss of one photon from that pulse. Noting that the energy of a photon is given by $h\nu_0$, an energy balance yields the change in pulse energy, $E_p^L(J)$,

$$\frac{dE_p^L}{dV} = -h\nu_0 N_T W_{12} \Delta\nu_{1/2}^L. \quad (46)$$

Substituting for the rate coefficient for stimulated absorption using Eq. (30b), we obtain

$$\frac{dE_p^L}{dV} = -\frac{g_2 \ln\left(\frac{1}{\sqrt{2}-1}\right) c^2 A_{21} E_p^L N_T}{g_1 2\pi^2 D^2 \nu_0^2 \Delta\nu_{1/2}^L}. \quad (47)$$

As shown, the temporal pulsewidth cancels out of the energy balance. Applying Eq. (30a), Eq. (47) reduces to

$$\frac{dI^L}{I^L} = -\frac{g_2 \ln\left(\frac{1}{\sqrt{2}-1}\right) c^2 A_{21} N_T}{g_1 8\pi\nu_0^2 \Delta\nu_{1/2}^L} dz. \quad (48)$$

Integration yields a Beer-Lambert attenuation expression.⁹ Thus while the use of picosecond pulses substantially changes the form of the rate equations, the absorption expression remains unchanged. The conclusion is limited, of course, to the low laser irradiance limit. Because saturation is purposely avoided in our experiments,⁵ the case of saturation need not be considered.

VIII. Absorbance for Picosecond Pulses

The transient absorption model is extended to the pump/probe configuration in Section IX. The pump/probe signal is derived in terms of a modulation depth, which can, in turn, be derived using the absorbance, α , which is now considered in this section. The spectral absorbance can be defined as^{25,32}

$$\alpha_\nu = \frac{I_\nu^L(0) - I_\nu^L(L)}{I_\nu^L(0)}. \quad (49)$$

The energy balance can also be applied on a spectral basis, yielding the spectral form of the Beer-Lambert attenuation equation.^{9,33} Substituting the equivalent spectral equation into Eq. (49), the spectral absorbance becomes

$$\alpha_\nu = 1 - \exp\left(-\frac{h\nu_0}{c} B_{12} Y(\nu) W_T L\right). \quad (50)$$

The total absorbance can be defined as the total absorbed irradiance divided by the total incident irradiance, or

$$\alpha = \frac{\int_{-\infty}^{\infty} \alpha_\nu I_\nu^L(0) d\nu}{I^L(0)}. \quad (51)$$

Since the laser linewidth is considerably larger than the linewidth of the medium,⁵ we may assume that the laser irradiance is constant at its line center value over the spectral profile of the medium. Thus employing Eqs (27) and (50), we obtain¹⁹

$$\alpha = \frac{\ln\left(\frac{1}{\sqrt{2}-1}\right)}{\Delta\nu_{1/2}^L} \int_{-\infty}^{\infty} \left[1 - \exp\left(-\frac{h\nu_0}{c} B_{12} Y(\nu) W_T L\right) \right] d\nu. \quad (52)$$

Assuming that $Y(\nu)$ is given by a Voigt profile,³⁴

$$\alpha = \frac{\ln\left(\frac{1}{\sqrt{2}-1}\right)}{\Delta\nu_{1/2}^L} \int_{-\infty}^{\infty} \left[1 - \exp\left(-\frac{h\nu_0 B_{12} N_T L}{c} \frac{2\sqrt{\ln 2}}{\sqrt{\pi}(\Delta\nu_{1/2})_D} V(\zeta_D, a) \right) \right] d\nu. \quad (53)$$

where $(\Delta\nu_{1/2})_D$ is the FWHM Doppler-broadened linewidth, ζ_D has been defined as

$$\zeta_D = 2\sqrt{\ln 2} \left(\frac{\nu - \nu_0}{(\Delta\nu_{1/2})_D} \right), \quad (54a)$$

the natural damping ratio has been defined as,³⁵

$$a = \sqrt{\ln 2} \frac{(\Delta\nu_{1/2})_C}{(\Delta\nu_{1/2})_D}, \quad (54b)$$

and the Voigt function is given by³⁴

$$V(\zeta_D, a) = \frac{a}{\pi} \int_{-\infty}^{\infty} \frac{\exp(-y^2) dy}{a^2 + (\zeta_D - y)^2}. \quad (54c)$$

For small optical depths $N_T L$, the optically thin limit can be shown to take the form²⁵

$$\alpha^{\text{THIN}} = \frac{\ln\left(\frac{1}{\sqrt{2}-1}\right) g_2 c^2 A_{21} N_T L}{\Delta\nu_{1/2}^L g_1 8\pi\nu_0^2}, \quad (55)$$

and for optically thick conditions, the absorbance becomes^{25,35-37}

$$\alpha^{\text{THICK}} = \frac{\ln\left(\frac{1}{\sqrt{2}-1}\right)}{\Delta\nu_{1/2}^L} \left[\frac{g_2 c^2 A_{21} (\Delta\nu_{1/2})_C N_T L}{g_1 4\pi\nu_0^2} \right]^{1/2}. \quad (56)$$

These two limits serve as a convenient means of defining the end of the linear absorption regime; defining this as the optical depth for which Eq. (55) intersects Eq. (56), the critical optical depth becomes

$$(N_T L)^* = \left(\frac{g_1}{g_2} \right) \frac{16\pi\nu_0^2 (\Delta\nu_{1/2})_C}{c^2 A_{21}}. \quad (57)$$

Using values from Tables I and II for our example of the atomic sodium D_2 line, the critical optical depth becomes $3.2 \times 10^{11} \text{ cm}^{-2}$. This is the upper limit for which pump/probe measurements can be assumed to be of practical use. For an interaction length of 1 cm,⁵ the maximum measurable sodium concentration becomes $3.2 \times 10^{11} \text{ cm}^{-3}$. Using the above absorbance expressions, along with our previous analysis of picosecond laser-excitation dynamics, we will now extend our model to the pump/probe configuration.

IX. Absorption in the Pump/Probe Configuration

A model that predicts the modulation of a probe laser from a pump-induced population will now be developed. This will allow an estimate of the minimum population that can be detected using picosecond pump/probe absorption spectroscopy. The model will then be modified to include the ASOPS technique for measuring excited-state lifetimes.

The model can be extended to a pump/probe experiment using the geometry of Fig. 5.³⁸ Here, the pump and probe beams are assumed to be cylinders with a diameter equal to the focal diameter. The absorption pathlength, L , corresponds to one side of the parallelogram formed where the beams cross. For the present calculations, the excitation scheme of Fig. 1(a) is chosen. Identical pulsewidths are assumed for each laser, and both laser repetition frequencies, f^L , are equal, as for previous pump/probe studies using synchronously mode-locked dye lasers.^{4,39}

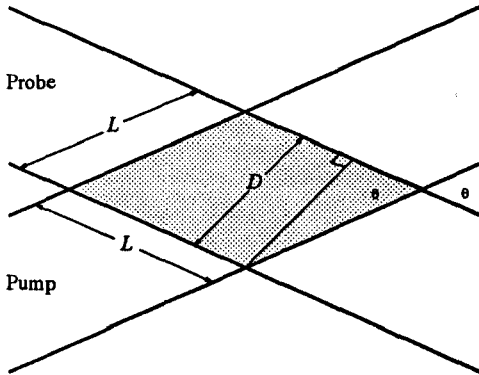


Fig. 5 Crossed-beam geometry utilized for pump/probe absorption mode.³⁸

When a pump pulse passes through the interaction volume, Eq. (35) indicates that the excited-state population becomes $N_2^{\text{pump}} = N_T \Delta_{12}^L W_{12}$. From Eq. (29) and (30a) this can be expressed as

$$N_2^{\text{pump}} = \left(\frac{g_2}{g_1} \right) \frac{\ln \left(\frac{1}{\sqrt{2}-1} \right) c^2 A_{21} \Delta_{12}^L N_T f^{\text{pump}}}{8\pi h \nu_{12}^3 \Delta \nu_{12}^L} \quad (58)$$

Substituting N_2^{pump} into Eq. (55) for optically-thin absorbance between levels 2 and 3, the probe modulation becomes

$$\alpha_{\text{mod}} = \left(\frac{g_3}{g_1} \right) \left[\ln \left(\frac{1}{\sqrt{2}-1} \right) \right]^2 \frac{c^4 A_{21} A_{32} \Delta_{12}^L f^{\text{pump}} N_T L}{64\pi^2 h \nu_{12}^3 \nu_{23}^2 (\Delta \nu_{12}^L)^2} \quad (59)$$

This can be expressed in terms of the pump laser power as

$$\alpha_{\text{mod}} = \left(\frac{g_3}{g_1} \right) \left[\ln \left(\frac{1}{\sqrt{2}-1} \right) \right]^2 \frac{c^4 A_{21} A_{32} P_{\text{pump}} N_T L}{16\pi^3 D^2 h \nu_{12}^3 \nu_{23}^2 f^L (\Delta \nu_{12}^L)^2} \quad (60)$$

Now suppose the pump is tuned to the $3S_{1/2} \rightarrow 3P_{3/2}$ transition of sodium, while the probe is tuned to the $3P_{3/2} \rightarrow 4D_{5/2}$ transition. For the latter transition, spectroscopic constants have been compiled in Table IV. Using the appropriate parameters from Tables II and IV, along with 1 mW of pump laser power (to preclude saturation), an absorbance of $3.6 \times 10^{-13} \text{ cm}^2 N_T L$ is predicted. For a 2.9° crossing angle,⁵ the effective path length becomes 0.152 cm, for which $\alpha_{\text{mod}} = 5.1 \times 10^{-14} \text{ cm}^3 N_T$. For high frequency modulation, with both pump and probe lasers operating at the same repetition frequency, a

minimum modulation depth of approximately 10^{-8} can be detected.⁴⁰ This corresponds to a minimum detectable population of $N_T = 2.0 \times 10^5 \text{ cm}^{-3}$. Note that this value corresponds to a 1-second time constant for detection using a lock-in amplifier.⁴⁰ Our objective is to take data on the time scale of $\sim 1 \text{ ms}$,⁵ so that our detection limit will be less optimistic.

Table IV Spectroscopic quantities utilized in many of the calculations in this paper. The spectroscopic quantities are for the D -lines of atomic sodium.¹⁸ Levels 1, 2, and 3 denote the $3S_{1/2}$, $3P_{3/2}$ and $4D_{5/2}$ levels, respectively.

g_2	4
g_3	6
g_1	2
A_{21}	$6.13 \times 10^7 \text{ s}^{-1}$
A_{23}	$1.23 \times 10^7 \text{ s}^{-1}$
ν_{12}	$5.0934 \times 10^{14} \text{ s}^{-1}$
ν_{23}	$5.2741 \times 10^{14} \text{ s}^{-1}$

A considerably more favorable prediction results if both beams are tuned to coincide with the D_2 line. In this case, α_{mod} will have a contribution from two sources, which can be conveniently derived by again applying the conservation of energy. One contribution is gain from $3P_{3/2} \rightarrow 3S_{1/2}$ stimulated emission. This gain modulation is given by

$$\frac{dE_p^{\text{probe}}}{dV} = h \nu_{12} N_2^{\text{pump}} W_{21}^{\text{probe}} \Delta_{12}^L, \quad (61)$$

where N_2^{pump} is given by Eq. (58). The other contribution arises from a decrease in ground-state absorption caused by a pump-induced reduction in the ground-state population density. This "apparent gain" term can be expressed as

$$\frac{dE_p^{\text{probe}}}{dV} = h \nu_{12} N_2^{\text{pump}} \Delta_{12}^L W_{12}^{\text{probe}}. \quad (62)$$

Summing contributions,

$$\frac{dE_p^{\text{probe}}}{dV} = h \nu_{12} N_2^{\text{pump}} \Delta_{12}^L (W_{12}^{\text{probe}} + W_{21}^{\text{probe}}) = \left(1 + \frac{g_1}{g_2} \right) h \nu_{12} N_2^{\text{pump}} \Delta_{12}^L W_{12}^{\text{probe}}. \quad (63)$$

Substituting from Eq. (30),

$$\frac{dE_p^{\text{probe}}}{dV} = \left(1 + \frac{g_2}{g_1} \right) \frac{\ln \left(\frac{1}{\sqrt{2}-1} \right) c^2 A_{21} N_2^{\text{pump}} E_p^{\text{probe}}}{2\pi^2 D^2 \nu_{12}^2 \Delta \nu_{12}^L}. \quad (64)$$

Applying Eq. (30a), and eliminating the differential volume in favor of the differential pathlength,

$$\frac{dI^{\text{probe}}}{I^{\text{probe}}} = \left(1 + \frac{g_2}{g_1} \right) \frac{\ln \left(\frac{1}{\sqrt{2}-1} \right) c^2 A_{21} N_2^{\text{pump}}}{8\pi \nu_{12}^2 \Delta \nu_{12}^L} dz. \quad (65)$$

Note that for each contribution, α_{mod} will be negative if the convention of Eq. (49) is followed. Kneisler (1990)³³ included a discrete variable that could take on a value of ± 1 depending on whether the modulation resulted from stimulated emission or from absorption. Albeit, no such variable is used here, and the negative sign will be dropped in these calculations, although the gain or loss taking place should be noted. Solving the differential equation, we obtain

$$I^{\text{probe}}(L) = I^{\text{probe}}(0) \exp \left[\left(1 + \frac{g_2}{g_1} \right) \frac{\ln \left(\frac{1}{\sqrt{2}-1} \right) c^2 A_{21} N_2^{\text{pump}} L}{8\pi \nu_{12}^2 \Delta \nu_{12}^L} \right], \quad (66)$$

which results in a modulation depth (optically thin) of

$$\alpha_{\text{mod}} = \left(1 + \frac{g_2}{g_1} \right) \frac{\ln \left(\frac{1}{\sqrt{2}-1} \right) c^2 A_{21} N_2^{\text{pump}} L}{8\pi \nu_{12}^2 \Delta \nu_{12}^L}. \quad (67)$$

Substituting from Eq. (58), and converting to average power

$$\alpha_{\text{mod}} = \left(\frac{g_2}{g_1} \right) \left(1 + \frac{g_2}{g_1} \right) \left[\ln \left(\frac{1}{\sqrt{2}-1} \right) \right]^2 \frac{c^4 A_{21}^2 P_{\text{pump}} N_T L}{16\pi^3 D^2 h \nu_{12}^3 \nu_{23}^2 f^L (\Delta \nu_{12}^L)^2}. \quad (68)$$

Using the values of Tables I and II, along with a 1-mW pump beam crossed at 2.9° with the probe, a detection limit of $N_T = 6.1 \times 10^4 \text{ cm}^{-3}$ is found for a modulation depth of 10^8 . This value is similar to the experimentally-obtained detection limit of $6.5 \times 10^4 \text{ cm}^{-3}$ reported by Langley *et al.*⁴ for the $2S_{1/2} \rightarrow 2P_{1/2,3/2}$ transition of atomic lithium.

The eventual application of pump/probe spectroscopy in a practical measurement scheme would be to detect OH. For the $Q_1(9)$ line of the $A^2\Sigma^+(v'=0) \leftrightarrow X^2\Pi(v''=0)$ transition at 2000 K, the Boltzmann fraction is 53.5, the detection frequency ν_0 is $9.7 \times 10^{14} \text{ sec}^{-1}$, and A_{21} is $6.36 \times 10^5 \text{ sec}^{-1}$.³⁴ Using the theory of Section VI, the average power required to saturate this transition with a 20-psec pulse is found to be 900 mW. Thus, the maximum available UV power for our laser systems can be used. This value happens to be approximately 1 mW.^{33,41} Using a 1-mW pump power in Eq. (68), a probe modulation of $\alpha_{\text{mod}} = 1.5 \times 10^{-18} \text{ cm}^2 N_T L$ is obtained. For an effective interaction path of $L = 0.152 \text{ cm}$, and a modulation depth of 10^8 , we estimate a detection limit of $N_{\text{OH}} = 2.3 \times 10^{12} \text{ cm}^{-3}$. Noise on the frequency-doubled output of a synchronously mode-locked dye laser is substantially larger than that on the fundamental output.^{19,42} Thus 10^8 may not be a realistic minimum detectable modulation depth; if so, detection of OH will be a difficult proposition. From this calculation, it is also easy to see why previous attempts at obtaining an OH ASOPS signal were not successful.³³ It has been noted that at low frequencies, the UV noise could be over 10^5 times larger than the shot-noise limit.^{19,42} This, coupled with the wide-band nature of the ASOPS method, indicates that significant improvements in the detection scheme will be necessary.⁵

Langley *et al.*⁴ used an electrooptic modulator in their pump laser. In this case, the modulator will not impart a 100% modulation depth at the fundamental of the modulation frequency, as is implicitly assumed in the above calculations. The detection limits associated with conventional pump/probe spectroscopy are thus inherently under-predicted because of this assumption. On the other hand, the pump and probe lasers of the ASOPS instrument both have modulation depths of 100% at $\sim 82 \text{ MHz}$. Thus where the beams overlap, the peak ASOPS signal will be well-represented by the above calculations. However, the ASOPS electronic bandwidth is much wider than assumed above. Moreover, the noise is far worse than that of the shot-noise limit when the temporal ASOPS signal is detected in our experiments.⁵ These facts should be kept in mind when judging the results of the above calculations.

A. ASOPS Absorption Model

Our experiments utilize the ASOPS detection scheme.⁵ Unlike the conventional pump/probe instrument, the ASOPS technique relies on two lasers with different repetition frequencies. The sodium atoms mix these frequencies to produce a difference, or beat, frequency which is then synchronously detected on an oscilloscope. This eliminates the need for amplitude modulation of either beam. The frequency difference also causes each probe pulse to be delayed in time relative to the pump pulse train by a constantly increasing duration. As a result, the temporal ASOPS signal, as seen on an oscilloscope, allows the lifetime of the excited state to be measured directly without an optical delay line. Hence, additional theory must now be included to account for the presence of temporal decays. This theory is also necessary for measuring lifetimes using a conventional pump/probe instrument.^{4,39}

After excitation by a pump pulse, the excited-state population will again be given by Eq. (58). In the absence of a probe pulse, this population will decay exponentially following Eq. (10), at a rate governed by

$$N_2(t) = N_2^{\text{pump}} \exp[-(Q+A)t] = \left(\frac{g_2}{g_1}\right) \frac{\ln\left(\frac{1}{\sqrt{2}-1}\right) c^2 A_{21} \Delta t_{1/2}^L N_T I^{\text{pump}}}{8\pi h \nu_{12}^3 \Delta \nu_{1/2}^2} \exp[-(Q+A)t]. \quad (69)$$

Assuming that the pump/probe configuration follows Fig. 1(a), Eq. (59) yields a probe-beam modulation of

$$\alpha_{\text{mod}}(t) = \left(\frac{g_3}{g_1}\right) \left[\ln\left(\frac{1}{\sqrt{2}-1}\right)\right]^2 \frac{c^4 A_{21} A_{32} \Delta t_{1/2}^L I^{\text{pump}} N_T L}{64\pi^2 h \nu_{12}^3 \nu_{23}^2 (\Delta \nu_{1/2}^2)^2} \exp[-(Q+A)t]. \quad (70)$$

The overall detection efficiency, η_d (volt- cm^{-3}/W), is now introduced to account for the optical and electronic detection characteristics. Noting that the photodetector output will be proportional to the amount of absorbed light at the modulation frequency, the instantaneous ASOPS signal can be written

$$S(t) = \eta_d \alpha_{\text{mod}}(t) I^{\text{probe}}. \quad (71)$$

Substituting from Eq. (70), the pump/probe model for a two-level absorber gives

$$S(t) = \eta_d \left(\frac{g_3}{g_1}\right) \left[\ln\left(\frac{1}{\sqrt{2}-1}\right)\right]^2 \frac{c^4 A_{21} A_{32} \Delta t_{1/2}^L I^{\text{pump}} N_T L}{64\pi^2 h \nu_{12}^3 \nu_{23}^2 (\Delta \nu_{1/2}^2)^2} \exp[-(Q+A)t]. \quad (72)$$

In terms of laser power, Eq. (72) can be expressed as

$$S(t) = \eta_d \left(\frac{g_3}{g_1}\right) \left[\ln\left(\frac{1}{\sqrt{2}-1}\right)\right]^2 \frac{c^4 A_{21} A_{32} P_{\text{AVE}}^{\text{pump}} P_{\text{AVE}}^{\text{probe}} N_T L \exp[-(Q+A)t]}{4\pi^2 D^4 h \nu_{12}^3 \nu_{23}^2 I^{\text{pump}} I^{\text{probe}} \Delta t_{1/2}^L (\Delta \nu_{1/2}^2)^2}. \quad (73)$$

The linear dependence of the ASOPS signal on the pump and probe beam power has been experimentally verified for atomic sodium excitation in an atmospheric-pressure hydrocarbon flame.³ A curve fit to Eq. (73) will yield Q , which can be used to correct for the effects of quenching.

The simplicity of the quenching correction scheme is lost when a multilevel atom or molecule is detected.³ A prime example is atomic sodium, for which level 2 must be split into two individual components to account for the presence of the $3P$ doublet. Levels 1, 2, and 3 correspond to the $3S_{1/2}$, $3P_{1/2}$, and $3P_{3/2}$ states, respectively. The pump beam resonantly excites either the $3S_{1/2} \rightarrow 3P_{1/2}$ transition or the $3S_{1/2} \rightarrow 3P_{3/2}$ transition. The probe will, in this example, be allowed to connect either the $3P_{1/2}$ or $3P_{3/2}$ level to a level of higher energy, such as the $5S_{1/2}$ or the $4D_{3/2,5/2}$ levels (denoted as level 4). The unfortunate consequence of the third level is the introduction of a second unknown collisional parameter, the doublet mixing rate coefficient.

Consider the specific case of a pump laser tuned to the $3S_{1/2} \rightarrow 3P_{3/2}$ transition, with the probe laser being tuned to the $3P_{3/2} \rightarrow 5S_{1/2}$ transition. Here, the pump-induced excited-state population will again be given by Eq. (58). However, Eq. (69) will no longer be applicable. From Eq. (26b), with all terms pertaining to N_2 being zero, the suitable equation becomes

$$N_3(t) = \frac{2}{3} N_3^{\text{pump}} \left\{ \exp[-(Q+A)t] + \frac{1}{2} \exp[-(Q+A+3Q_{32})t] \right\}. \quad (74)$$

Substitution from Eq. (58) with appropriate changes in notation yields

$$N_3(t) = \frac{2}{3} \left(\frac{g_3}{g_1}\right) \frac{\ln\left(\frac{1}{\sqrt{2}-1}\right) c^2 A_{31} \Delta t_{1/2}^L N_T I^{\text{pump}}}{8\pi h \nu_{13}^3 \Delta \nu_{1/2}^2} \times \left\{ \exp[-(Q+A)t] + \frac{1}{2} \exp[-(Q+A+3Q_{32})t] \right\}. \quad (75)$$

Applying Eqs. (59) and (71) with appropriate changes in notation, the corresponding ASOPS signal is given by

$$S(t) = \frac{2}{3} \eta_d \left(\frac{g_4}{g_1}\right) \left[\ln\left(\frac{1}{\sqrt{2}-1}\right)\right]^2 \frac{c^4 A_{31} A_{43} \Delta t_{1/2}^L I^{\text{pump}} N_T L}{64\pi^2 h \nu_{13}^3 \nu_{24}^2 (\Delta \nu_{1/2}^2)^2} \times \left\{ \exp[-(Q+A)t] + \frac{1}{2} \exp[-(Q+A+3Q_{32})t] \right\}, \quad (76)$$

which can be expressed in terms of laser power using the assumptions of Section IV.

As shown, there are now three unknowns (N_T , Q , and Q_{32}). Hence a second measurement is required. For instance, the probe could be switched to instead connect the $3P_{1/2} \rightarrow 5S_{1/2}$ transition, for which Eq. (26a) predicts

$$N_2(t) = \frac{1}{3} N_3^{\text{pump}} \{ \exp[-(Q+A)t] - \exp[-(Q+A+3Q_{32})t] \}, \quad (77)$$

resulting in the temporal signal

$$S(t) = \frac{1}{3} \eta_d \left(\frac{g_3}{g_1}\right) \left(\frac{g_4}{g_2}\right) \left[\ln\left(\frac{1}{\sqrt{2}-1}\right)\right]^2 \frac{c^4 A_{31} A_{42} \Delta t_{1/2}^L I^{\text{pump}} N_T L}{64\pi^2 h \nu_{13}^3 \nu_{24}^2 (\Delta \nu_{1/2}^2)^2} \times \{ \exp[-(Q+A)t] - \exp[-(Q+A+3Q_{32})t] \}. \quad (78)$$

An obvious disadvantage to this procedure is that two different ASOPS signals must be obtained. The objective of our research is to measure concentrations within the time scale of turbulence. This will not be possible if two separate lifetime measurements are necessary. Fiechtner *et al.*³ fitted their ASOPS decay by assuming a literature value for the ratio Q/Q_{32} . The value of this ratio will not always be known. Clearly, a better method is needed to obtain meaningful ASOPS measurements.

B. Dual-Beam ASOPS

Because of the possible presence of coherent transients, some previous ASOPS decays were accompanied by an anomalous signal at the end of the free temporal range.²⁶ In these early measurements, both beams were tuned to the same transition of atomic sodium. We subsequently found that the anomalous signal could be avoided by using the detection scheme of Fig. 1(b). Thus a second study utilized this scheme exclusively.³ However, as described above, this detection method is of limited value, because of the two unknowns, Q and Q_{32} . Moreover, the SNR will be much less than that of the first experiments,²⁶ because the probe-coupled transitions have a smaller absorption cross section.¹⁹

It might be more valuable to ignore the presence of coherent transients, and tune both beams to the D_2 transition, thereby improving the SNR. In this case, derivation of the resulting ASOPS modulation is slightly more complicated than above, since the signal is now the sum of two contributions. The first is due to stimulated emission by the probe, given by

$$\frac{dE_p^{\text{probe}}}{dV} = h\nu_{13}N_3(t)\Delta\epsilon_{12}^L W_{31}^{\text{probe}}. \quad (79)$$

The second contribution results from the apparent gain that arises from an absence of ground state atoms. These atoms are excited by the pump, and can no longer absorb the probe. This contribution is given by

$$\frac{dE_p^{\text{probe}}}{dV} = h\nu_{13}N_3(t)\Delta\epsilon_{12}^L W_{13}^{\text{probe}}. \quad (80)$$

Summing Eqs. (79) and (80), the overall energy balance becomes

$$\frac{dE_p^{\text{probe}}}{dV} = h\nu_{13}N_3(t)\Delta\epsilon_{12}^L (W_{31}^{\text{probe}} + W_{13}^{\text{probe}}) = \left(1 + \frac{g_1}{g_3}\right) h\nu_{13}N_3(t)\Delta\epsilon_{12}^L W_{13}^{\text{probe}}. \quad (81)$$

The time-varying, pump-induced population is considered by substituting from Eq. (26b), yielding the expression

$$\frac{dE_p^{\text{probe}}}{dV} = \frac{2}{3} \left(1 + \frac{g_1}{g_3}\right) h\nu_{13}\Delta\epsilon_{12}^L W_{13}^{\text{probe}} N_3^{\text{pump}} \times \left\{ \exp[-(Q+A)\tau] + \frac{1}{2} \exp[-(Q+A+3Q_{32})\tau] \right\}. \quad (82)$$

Substituting from Eqs. (28) and (30a), the energy balance can be converted to an expression in terms of laser irradiance, which takes the form

$$\frac{dI^{\text{probe}}}{dz} = \frac{2}{3} \left(1 + \frac{g_3}{g_1}\right) \ln\left(\frac{1}{\sqrt{2}-1}\right) \frac{c^2 A_{31} N_3^{\text{pump}} I^{\text{probe}}}{8\pi\nu_{13}^2 \Delta\nu_{12}^L} \times \left\{ \exp[-(Q+A)\tau] + \frac{1}{2} \exp[-(Q+A+3Q_{32})\tau] \right\}. \quad (83)$$

The corresponding temporal ASOPS signal then becomes¹⁹

$$S(t) = \frac{2}{3} \eta_d \frac{g_3}{g_1} \left(1 + \frac{g_3}{g_1}\right) \left[\ln\left(\frac{1}{\sqrt{2}-1}\right) \right]^2 \frac{c^4 A_{31}^2 \Delta\epsilon_{12}^L I^{\text{pump}} I^{\text{probe}} N_T L}{64\pi^2 h\nu_{13}^3 (\Delta\nu_{12}^L)^2} \times \left\{ \exp[-(Q+A)\tau] + \frac{1}{2} \exp[-(Q+A+3Q_{32})\tau] \right\}. \quad (84)$$

While this configuration yields a larger signal, the resulting decay has the same disadvantage of two unknown collisional parameters.

However, consider the case for which the pump is tuned to the D_1 line, while the probe is tuned to the D_2 line. Summing the contributions from stimulated emission and apparent gain, respectively, an energy balance yields

$$\begin{aligned} \frac{dE_p^{\text{probe}}}{dV} &= h\nu_{13}N_3(t)\Delta\epsilon_{12}^L W_{31}^{\text{probe}} + h\nu_{13}N_2(t)\Delta\epsilon_{12}^L W_{13}^{\text{probe}} \\ &= h\nu_{13}\Delta\epsilon_{12}^L W_{13}^{\text{probe}} \left[\frac{g_1}{g_3} N_3(t) + N_2(t) \right]. \end{aligned} \quad (85)$$

Substituting from Eqs. (26a) and (26b),

$$\frac{dE_p^{\text{probe}}}{dV} = \frac{1}{3} h\nu_{13}\Delta\epsilon_{12}^L W_{13}^{\text{probe}} N_2^{\text{pump}} \left[2\exp[-(Q+A)\tau] + \exp[-(Q+A+3Q_{32})\tau] \right]. \quad (86)$$

The corresponding ASOPS signal can be shown to take the form¹⁹

$$S(t) = \frac{2}{3} \eta_d \left[\ln\left(\frac{1}{\sqrt{2}-1}\right) \right]^2 \frac{c^4 A_{21} A_{31} \Delta\epsilon_{12}^L I^{\text{pump}} I^{\text{probe}} N_T L}{64\pi^2 h\nu_{13}^3 (\Delta\nu_{12}^L)^2} \times \{2\exp[-(Q+A)\tau] + \exp[-(Q+A+3Q_{32})\tau]\}. \quad (87)$$

Eq. (87) contains the same two unknown collisional parameters. However, for this particular pump/probe configuration, both beams are modulated.⁵ Since the D_1 beam excites a different transition, the corresponding decay will be governed by an equation that differs from Eq. (87). By simultaneously detecting both beams, Q and Q_{32} can both be determined within the time scale of turbulence using a single measurement. In this case, both beams serve as the pump, and both beams serve as the probe. This method, which we call the dual-beam ASOPS method, has been experimentally demonstrated by our research group.⁵

The signal on the D_1 beam can be derived by again summing the contributions from stimulated emission and apparent gain, to obtain

$$\begin{aligned} \frac{dE_p^{\text{probe}}}{dV} &= h\nu_{12}N_2(t)\Delta\epsilon_{12}^L W_{21}^{\text{probe}} + h\nu_{12}N_3(t)\Delta\epsilon_{12}^L W_{12}^{\text{probe}} \\ &= h\nu_{12}\Delta\epsilon_{12}^L W_{12}^{\text{probe}} [N_2(t) + N_3(t)], \end{aligned} \quad (88)$$

where the quantities $g_1=g_2=2$ have been applied (Table I). Substituting from Eqs. (26a) and (26b),

$$\frac{dE_p^{\text{probe}}}{dV} = h\nu_{12}\Delta\epsilon_{12}^L W_{12}^{\text{probe}} N_3^{\text{pump}} \exp[-(Q+A)\tau]. \quad (89)$$

The corresponding ASOPS signal becomes

$$S(t) = \eta_d \left[\ln\left(\frac{1}{\sqrt{2}-1}\right) \right]^2 \frac{c^4 A_{21} A_{31} \Delta\epsilon_{12}^L I^{\text{pump}} I^{\text{probe}} N_T L}{64\pi^2 h\nu_{12}^3 (\Delta\nu_{12}^L)^2} \exp[-(Q+A)\tau]. \quad (90)$$

The simple exponential decay results from the equal degeneracies of the levels that are connected by the probe. Since Eq. (90) predicts an exponential decay in terms of only Q , the corresponding excitation scheme is used frequently in our experiments.⁵ This fortunate result may not be possible when detecting species other than sodium using dual-beam ASOPS. We are presently examining the possibility for diatomic flame species. Nevertheless, both Q and Q_{32} can still be obtained from a single measurement. This result is significant because it suggests that quenching-independent concentration measurements are possible within the time-scale of turbulence, in contrast to previous ASOPS studies.³

X. Coherent Transient Interferences

Quenching-independent concentration measurements are possible when $\Delta\nu_{12}^L \ll Q_{21}^{-1}$. However, this fact can also lead to the present of coherent transients. Careful consideration is necessary to prevent coherent effects from dominating the desired pump/probe signals. When coherent transients are important, the above rate-equation theory will not be valid. Instead, theory must be developed using the density matrix equations or the optical Bloch equations. Assuming that $\Delta\nu_{12}^L \ll Q_{21}^{-1}$, and applying the rotating-wave approximation, the optical Bloch formalism yields the following expression for a two-level absorber:⁴³

$$\frac{N_1^{\text{pump}}}{N_T} = -\cos\Theta, \quad (91)$$

where Θ is the flopping angle (radians), related to the Rabi frequency (s^{-1}) by $\Theta = \Omega \Delta\nu_{12}^L$. The Rabi frequency is given by^{43,44}

$$\Omega = \frac{2\pi\mu |E_0|}{h}, \quad (92)$$

where E_0 is the electric field strength ($\text{kg}\cdot\text{m}/\text{A}\cdot\text{s}^3$) and μ is the dipole moment ($\text{m}\cdot\text{s}\cdot\text{A}$). Note that Eq.'s (91) and (92) hold when the laser bandwidth is much smaller than the spectral width of the atoms. The opposite case holds in this investigation, although Eq.'s (91) and (92) provide a qualitative explanation of the difficulties that can arise from coherent transients. Various expressions for μ can be written in terms of A_{21} ,²² depending on the type and orientation of the polarizations of both the laser and the atoms. The electric field strength can be written in terms of the average laser power or the laser irradiance by⁴³

$$|E_0|^2 = \frac{2I^L}{\epsilon_0 c} = \frac{2P_{\text{AVE}}^L}{\epsilon_0 c A_c}, \quad (93)$$

where ϵ_0 is the dielectric constant of free space ($\text{A}^2\cdot\text{s}^4/\text{kg}\cdot\text{m}^3$). From Eqs. (91)–(93) it is clear that certain combinations of laser pulsewidth and irradiance will cause $\Theta=\pi/2, \pi, 3\pi/2$, etc., resulting in interesting coherent behavior. Moreover, strong irradiance will cause the population density N_2 to sinusoidally oscillate while the laser pulse is present in the flame. These cases will not be predicted by the rate equation analysis.

Nevertheless, the use of rate equations is justified if the coherence time of the laser is short compared to the pumping time.⁷ The coherence time is the reciprocal of the bandwidth,⁴⁵ and the pumping time is the reciprocal of the absorption probability.⁷ Thus our pump/probe model should hold if

$$W_{12} \ll \Delta\nu_{12}^L. \quad (94)$$

is satisfied.

For our bandwidth value of $1.58\times 10^{10}\text{s}^{-1}$, and assuming an equality in Eqn. (94), an average power of 420 μW is estimated. This could explain the negative artifact that we observed in previous ASOPS experiments, in which the laser power was greater than 10 mW. In this case, the artifact was probably caused by perturbed free induction decay (PFID).^{39,46,47} For cases in which the condition of Eqn. (94) is only moderately violated, coherent transient effects may not be important. The laser spatial profile will require that the interaction between the laser and atoms be averaged over different irradiances.⁷ Moreover, the value assumed for $\Delta\nu_{12}^L$ is estimated by assuming the laser pulses are perfectly transform-limited. Our laser pulses are not perfectly transform-limited, and thus the bandwidth of $1.58\times 10^{10}\text{s}^{-1}$ represents a minimum value.²⁴ In our present experiments⁵, we employ a 700- μW average power, and find that coherent effects are often negligible.

We have been able to obtain ASOPS signals in which the magnitude of coherent effects is negligible.⁵ For these signals, the present rate equation model remains a valid and useful tool for interpreting data.

XI. Conclusions

A model has been developed to predict practical operating limits using synchronously mode-locked dye lasers for picosecond pump/probe absorption spectroscopy. Particular limits considered are those caused by saturation and optical thickness. A minimum detectability is estimated corresponding to the shot-noise limit. This estimate corresponds well with the experimentally-observed detection limit of Jones and coworkers.⁴

For a 1-second integration time, we predict a detection limit for OH of $2.3 \times 10^{12}\text{cm}^{-3}$. However, for turbulent flames, we require a measurement time of ~ 1 ms; moreover, we have been unable to achieve the shot noise limit when using our laser systems.⁵ The detection of OH is also complicated by the notoriously low average power that our laser systems produce in the UV.⁴¹ New Ti:Sapphire laser technology allows two orders of magnitude more UV power,⁴⁸ which need not be attenuated, since the predicted saturation parameter for OH is ~ 900 mW. The modulation depth on the probe, and thus the detection limit would be improved by approximately two orders of magnitude as predicted using Eq. (68). Unfortunately, these lasers produce a minimum wavelength of ~ 350 nm, which falls above the spectral range necessary for OH excitation. However, we note that several diatomic species fall within the frequency-doubled Ti:Sapphire laser tuning range, including CH (${}^2\Delta\text{---}{}^2\pi$) at 431.5 nm and CN (${}^2\Sigma\text{---}{}^2\Sigma$) at 400.0 nm.⁴⁴

The pump/probe model has also been modified to include the problem of measuring excited-state lifetimes. For a three-level absorber such as atomic sodium, a new technique is developed which allows measurement of the lifetime in a single measurement. This is in contrast to our previous experiments with atomic sodium using the ASOPS instrument,³ in which a single measurement would not directly yield an estimate for Q . We call the new technique "dual-beam ASOPS". We report the first successful demonstration of dual-beam ASOPS in Part 2.⁵

Acknowledgments

The authors are extremely grateful for the advice of Professor Fred Lytle, Department of Chemistry, Purdue University. We also wish to thank Dr. Cam Carter, Sandia National Laboratories, Livermore, CA, and John Reisel, School of Mechanical Engineering, Purdue University, for their helpful discussions concerning OH spectroscopy. This work was sponsored by the U.S. Air Force Office of Scientific Research, Air Force Systems Command, under grant AFOSR-84-0323.

References

1. A. C. Eckbreth, *Laser Diagnostics for Combustion Temperature and Species*, Abacus Press, Cambridge, MA, 1988.
2. R. P. Lucht, in *Laser Spectroscopy and Its Applications*, L. J. Radziemski, R. W. Solarz and J. A. Paisner, eds., Marcel Dekker, Inc., New York, NY, 1987.
3. G. J. Fiechtner, G. B. King, N. M. Laurendeau and F. E. Lytle, *Appl. Opt.* **31**, 2849-2864 (1992).
4. R. A. Beaman, Ph.D. dissertation, (University of Wales, 1985); A. J. Langley, R. A. Beaman, J. Baran, A. N. Davies, W. J. Jones, *Opt. Lett.* **10**, 327-329 (1985); A. J. Langley, R. A. Beaman, A. N. Davies, W. J. Jones and J. Baran, *Chem. Phys.* **101**, 117-125 (1986); R. A. Beaman, A. N. Davies, A. J. Langley, W. J. Jones and J. Baran, *Chem. Phys.* **101**, 127-132 (1986); W. J. Jones, *J. Chem. Soc., Faraday Trans. 2* **83**, 693-705 (1987); W. Mallawaarachchi, A. N. Davies, R. A. Beaman, A. J. Langley, W. J. Jones, *J. Chem. Soc. Faraday Trans. 2* **83**, 707-722 (1987).
5. G. J. Fiechtner, G. B. King and N. M. Laurendeau, Part 2 of this paper. Parts 1 and 2 will be submitted to *Applied Optics*.
6. C. Th. J. Alkemade, *Spectrochim. Acta* **40B**, 1331-1368 (1985).
7. R. Altkorn and R. N. Zare, *Ann. Rev. Phys. Chem.* **35**, 265-289 (1984).
8. R. P. Lucht and N. M. Laurendeau, *Comb. Flame* **34**, 215-217 (1979).
9. R. M. Measures, *Laser Remote Sensing*, John Wiley & Sons, New York, NY, 1984.
10. M. Hercher, *Appl. Opt.* **6**, 947-954 (1967).
11. R. M. Measures, *J. Appl. Phys.* **39**, 5232-5245 (1968).
12. D. R. Olivares and G. M. Hieftje, *Spectrochim. Acta* **33B**, 79-99 (1978).
13. G. D. Boutilier, N. Omenetto and J. D. Winefordner, *Appl. Opt.* **19**, 1838-1843 (1980).
14. G. Zizak, J. D. Bradshaw and J. D. Winefordner, *Appl. Opt.* **19**, 3631-3639 (1980).
15. N. Omenetto, C. A. van Dijk and J. D. Winefordner, *Spectrochim. Acta* **37B**, 703-711 (1982).
16. R. J. Catollica, D. Stepowski, D. Puechberty and M. Cottureau, *J. Quant. Spectrosc. Radiat. Transfer* **32**, 363-370 (1984).
17. N. Omenetto, G. C. Turk, M. Rutledge and J. D. Winefordner, *Spectrochim. Acta* **42B**, 807-817 (1987).
18. O. Axner, M. Norberg and H. Rubinsztein-Dunlop, *Spectrochim. Acta* **44B**, 693-712 (1989).
19. G. J. Fiechtner, Ph.D. dissertation (Purdue University, West Lafayette, Indiana, 1992).

20. Y. Takubo, T. Okamoto and M. Yamamoto, *Appl. Opt.* **25**, 740-743 (1986).
21. R. A. Van Calcar, M. J. M. Van de Ven, B. K. Van Uitert, K. J. Biewenga, Tj. Hollander and C. Th. J. Alkemade, *J. Quant. Spectrosc. Radiat. Transfer* **21**, 11-18 (1979).
22. A. E. Siegman, *Lasers*, University Science Books, Mill Valley, CA, 1986.
23. C. J. Hooker, J. M. D. Lister and I. N. Ross, *Opt. Commun.* **80**, 375-380 (1991).
24. G. J. Blanchard and M. J. Wirth, *Opt. Commun.* **53**, 394-400 (1985).
25. C. Th. J. Alkemade, Tj. Hollander, W. Snelleman and P. J. Th. Zeegers, *Metal Vapours in Flames*, Pergamon Press, New York, NY (1982).
26. G. J. Fiechtner, Y. Jiang, G. B. King, N. M. Laurendeau, R. J. Kneisler and F. E. Lytle, *Twenty-Second Symposium (International) on Combustion*, The Combustion Institute, Pittsburgh, PA, 1988, pp. 1915-1921.
27. J. P. Bentley, *Principles of Measurement Systems*, Longman Scientific & Technical, Essex, England, 1988.
28. N. Omenetto, *Spectrochim. Acta* **37B**, 1009-1014 (1982).
29. D. Stepowski and M. J. Cottureau, *Appl. Opt.* **18**, 354-356 (1979); D. Stepowski and M. J. Cottureau, *Comb. Flame* **40**, 65-70 (1981); D. Stepowski and M. J. Cottureau, *J. Chem. Phys.* **74**, 6674-6679 (1981).
30. J. T. Salmon and N. M. Laurendeau, *Appl. Opt.* **24**, 65-72 (1985); J. T. Salmon and N. M. Laurendeau, *Appl. Opt.* **24**, 1313-1321 (1985).
31. R. P. Lucht, D. W. Sweeney, and N. M. Laurendeau, *Appl. Opt.* **19**, 3295-3300 (1980).
32. R. Siegel and J. R. Howell, *Thermal Radiation Heat Transfer*, Hemisphere Publishing Corporation, NY, 1981.
33. R. J. Kneisler, Ph.D. dissertation, (Purdue University, West Lafayette, Indiana, 1990).
34. R. P. Lucht, R. C. Peterson, and N. M. Laurendeau, *Fundamentals of Absorption Spectroscopy for Selected Diatomic Flame Radicals*, NSF PURDU-CL-78-06, Purdue University, West Lafayette, IN, October, 1978.
35. A. C. G. Mitchell and M. W. Zemansky, *Resonance Radiation and Excited Atoms*, Cambridge University Press, London, 1961.
36. A. Unsöld, Springer-Verlag, Berlin, 1955.
37. H. Hinnov, *JOSA* **47**, 151 (1957).
38. G. J. Blanchard and M. J. Wirth, *Anal. Chem.* **58**, 532-535 (1986).
39. B. A. Mann, Ph.D. dissertation, (University of Reading, Whiteknights, Reading, Berks, England, 1991).
40. J. P. Heritage, in *Advances in Laser Spectroscopy* 2, B. A. Garetz and J. R. Lombardi, eds., John Wiley & Sons Ltd., New York, NY, 1983, pp. 207-224.
41. G. J. Fiechtner, G. B. King, N. M. Laurendeau, R. J. Kneisler and F. E. Lytle, *Appl. Spectrosc.* **43**, 1286-1287 (1989).
42. D. Von der Linde, *Appl. Phys. B* **39**, 201-217 (1986).
43. P. W. Milonni and J. H. Eberly, *Lasers*, John Wiley & Sons, New York, NY, 1988.
44. J. W. Daily, *Appl. Opt.* **18**, 360-367 (1979).
45. P. Avan and C. Cohen-Tannoudji, *J. Phys. B* **10**, 155-170 (1977).
46. C. H. Brito Cruz, J. P. Gordon, P. C. Becker, R. L. Fork and C. V. Shank, *IEEE J. Quantum Electron.* **QE-24**, 261-264 (1988).
47. M. Joffe, D. Hulin, A. Migus, A. Antonetti, C. Benoit a la Guillaume, N. Peyghambarian, M. Lindberg and S. W. Koch, *Opt. Lett.* **13**, 276-278 (1988).
48. Advertisement No. 446, "Ti:Sapphire frequency doubler," Spectra-Physics Lasers, Mountain View, CA, in *Laser World Focus* **28**, 248 (1992).

PART 2:

Quantitative Concentration Measurements of Atomic Sodium in an Atmospheric Hydrocarbon Flame by Asynchronous Optical Sampling (ASOPS)

This paper contains a discussion of the first truly quantitative evaluation of the ASOPS method in a combustion environment. Atomic sodium is again detected. The absolute sodium number density is measured using atomic absorption spectroscopy (AAS). The AAS results are then compared with those obtained using the ASOPS method; close agreement is observed for the onset of optically-thick conditions. ASOPS data are taken at a beat frequency of 155.7 kHz with only 128 averages. The resulting potential collection time is sufficient for turbulent fluctuations of ~ 1 ms or less. The corresponding detection limit for a 1:1 SNR is measured. This limit is then used in conjunction with the picosecond pump/probe absorption model of Part 1 to estimate the minimum detectability for the hydroxyl radical. The quenching rate coefficient is obtained with a single measurement using the dual-beam ASOPS configuration, which we introduced in Part 1.

The purpose of this project is to make concentration measurements within the time scale of turbulence in high-pressure flames. As an example of the type of data that we hope to obtain, consider the study of Wrobel and Pratt,⁴ who excited atoms in a turbulent diffusion flame using a CW laser. The resulting fluorescence signal was analyzed recording power spectral densities (PSD's) from DC to 10 kHz, necessary as part of a complete turbulence experiment. However, the CW fluorescence signal is inversely proportional to the quenching rate coefficient, Q , introducing uncertainty into the data through fluctuations in the collisional environment.² We seek to overcome this difficulty by using picosecond pump/probe absorption spectroscopy. In particular, we demonstrate the quantitative use of the Asynchronous Optical Sampling (ASOPS) technique, which we describe below.

Previous ASOPS studies of atomic sodium in an atmospheric flame² served as an excellent demonstration of the technique. However, the resulting data were lacking in several respects:

- (1) Previous results were purely qualitative. Since absolute number densities were not known for these studies, it is not possible to make quantitative predictions about the detection of other species in different flames.
- (2) The results were obtained in a period that is much longer than that of relevant turbulent fluctuations. This limited previous studies to laminar flowfields.
- (3) Previous experiments were based on the excitation scheme of Fig. 1(b) of Part 1. This scheme eliminates the presence of unwanted anomalous signals that tend to appear when both beams are in resonance with ground-state atoms.³ However, the resulting signal depends on both the electronic quenching rate coefficient, Q , and the doublet mixing rate coefficient, Q_{32} , as shown in Eq. (78) of Part 1. Thus while the curve fit of previous ASOPS experiments happened to agree with literature values for Q and Q_{32} , such literature values will not normally be known. In this case, there will be an infinite number of possible curve fits.

Each of these difficulties is systematically eliminated in the present study.

I. Choice of a Pump/Probe Instrument

As demonstrated by Eq. (60) of Part 1, two pulse trains that overlap in space and time in a flame will enable quenching-independent concentration measurements. A practical implementation of this method is shown in Fig. 1, which contains a conventional pump/probe instrument.^{4,5} Since both the pump and probe beams are derived from the same actively mode-locked laser, both have the same repetition

frequency. Pulses are temporally overlapped where they cross in the flame using an optical delay line. The pump is amplitude modulated at a > 1 MHz, and the resulting probe modulation is synchronously detected using a high-frequency lock-in amplifier. The amplifier output can be Fourier-transformed to obtain PSD's. However, it is necessary to frequency-double the output when detecting diatomic flame species such as OH. Since the modulator cannot be used with an ultraviolet (UV) beam, the dye-laser output must be split into two portions and then frequency-doubled. The resulting average power will be in the tens of microwatts,⁶ much too small for detection of OH (Part 1).

To obviate this problem, we have evaluated the pump/probe instrument of Fig. 2. Here, two actively mode-locked Nd:YAG lasers are frequency-doubled, and the output is used to synchronously pump two dye lasers. The mode-lockers of both lasers are driven with the same frequency synthesizer (PTS 160), so that the ~ 82 -MHz repetition rates of both laser systems are identical. This requires adjustments to match the cavity lengths of both Nd:YAG lasers. To provide a convenient means of temporally overlapping the pulses from each laser in the interaction volume, a voltage-controlled phase shifter (Merrimac PEW-3-60) is placed between the frequency synthesizer and the mode-locker of the pump laser. A variable DC voltage source is used to adjust the phase between the two laser systems. Additional phase adjustments are made with an optical delay line, through which the pump laser beam passes. The pump beam also passes through a 4-kHz chopper, since this is easier to use than an electrooptic modulator. When a low-frequency lock-in amplifier is used to demodulate the probe signal, an impressive SNR results, even though the 4-kHz modulation frequency is located on top of sizeable baseband laser noise.⁷ Unfortunately, long-term drift of the phases of each laser pulse train requires that constant adjustments of the optical delay line be made. The chief advantage of this scheme is that at least 1 mW of average UV power is available for both the pump and probe beams.

To retain the 1-mW average UV power, and eliminate the problem of temporally overlapping two pulse trains that emanate from two actively mode-locked lasers, we chose to again conduct experiments using the ASOPS instrument. In this case, each laser is actively mode-locked using a separate frequency synthesizer. The synthesizers are operated in a phase-locked, master-slave configuration in which the pump laser oscillator is also used as the reference oscillator for the probe laser. The lasers are then operated at different repetition frequencies, f_{pump} and f_{probe} . Thus where the pump and probe beams pass through the sample, a beat frequency of $f_{\text{beat}} = f_{\text{pump}} - f_{\text{probe}}$ will be impressed onto the probe laser, eliminating the need for amplitude modulation of the pump laser. More importantly, a controlled repetitive phase walkout of the pump and probe pulse trains occurs in the interaction volume.

The automatic ASOPS phase walkout eliminates the need for an optical delay line or electronic phase shifter, as demonstrated in Fig. 3(a), which contains the excited-state population produced by several pump pulses and the superimposed temporal position of several probe pulses. Each successive probe pulse is delayed in time (relative to the pump pulse train) by a constantly increasing duration which is determined by the beat frequency of the system. Thus each probe pulse samples the excited-state population at a slightly later time than the preceding probe pulse. Fig. 3(b) illustrates the change in probe laser intensity that occurs upon stimulated emission from the excited-state population in Fig. 3(a). The net effect of the ASOPS technique is that a small amplitude waveform, which is directly related to the fluorescence decay of the species under study, is impressed onto the probe laser intensity. In essence, a temporal transformation of the excited-state decay is performed with the time scaled by the factor $f_{\text{pump}}/(f_{\text{pump}} - f_{\text{probe}})$. The process automatically repeats at the period of the ASOPS instrument, given by $1/f_{\text{beat}}$. The ASOPS technique is thus the optical analogue of the sampling oscilloscope. Consequently, the ASOPS instrument potentially allows a large number of averages to be obtained in a time less than that of most rapid turbulent fluctuations (~ 1 ms).

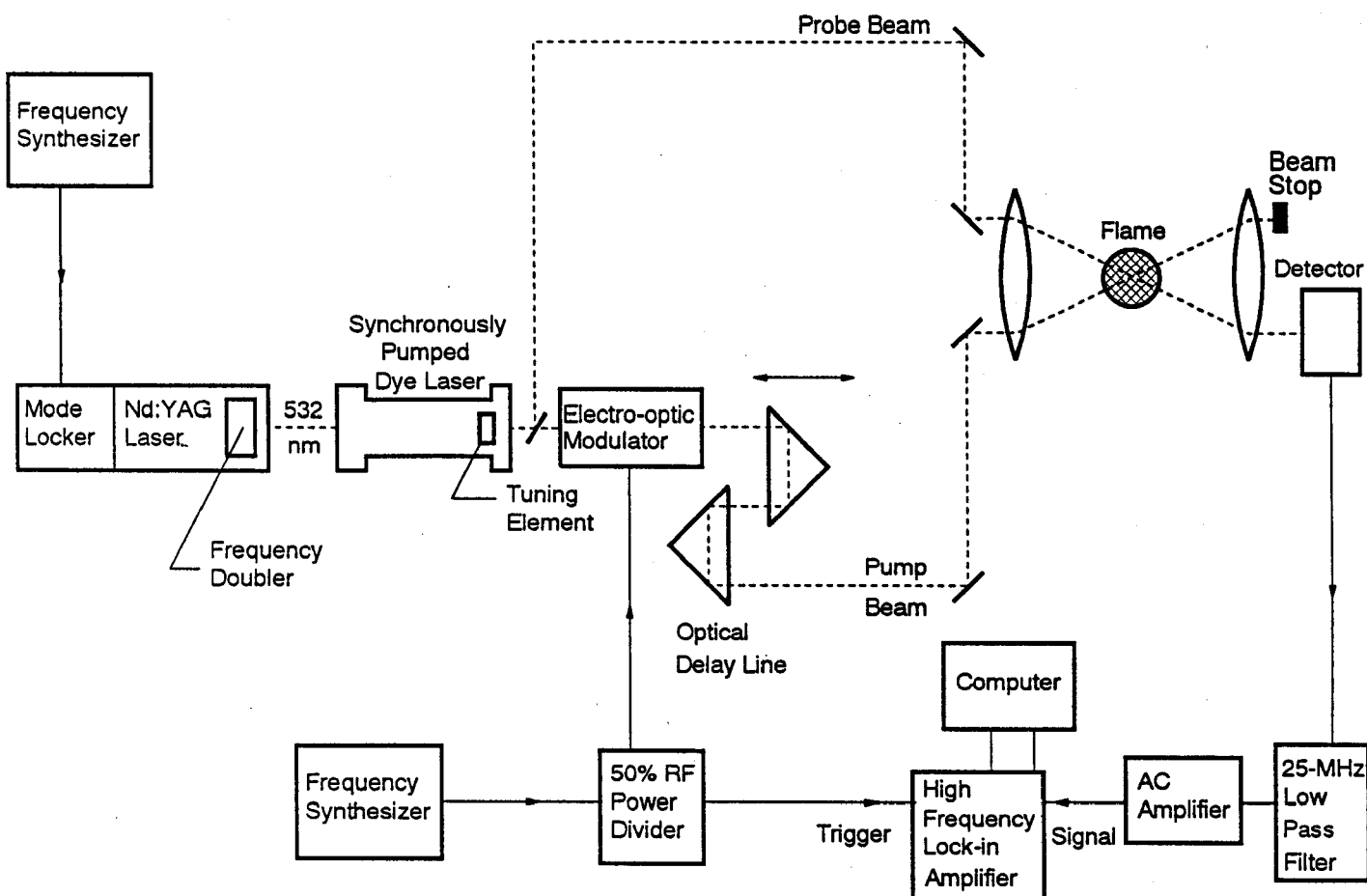


Fig. 1 Conventional pump/probe instrument.

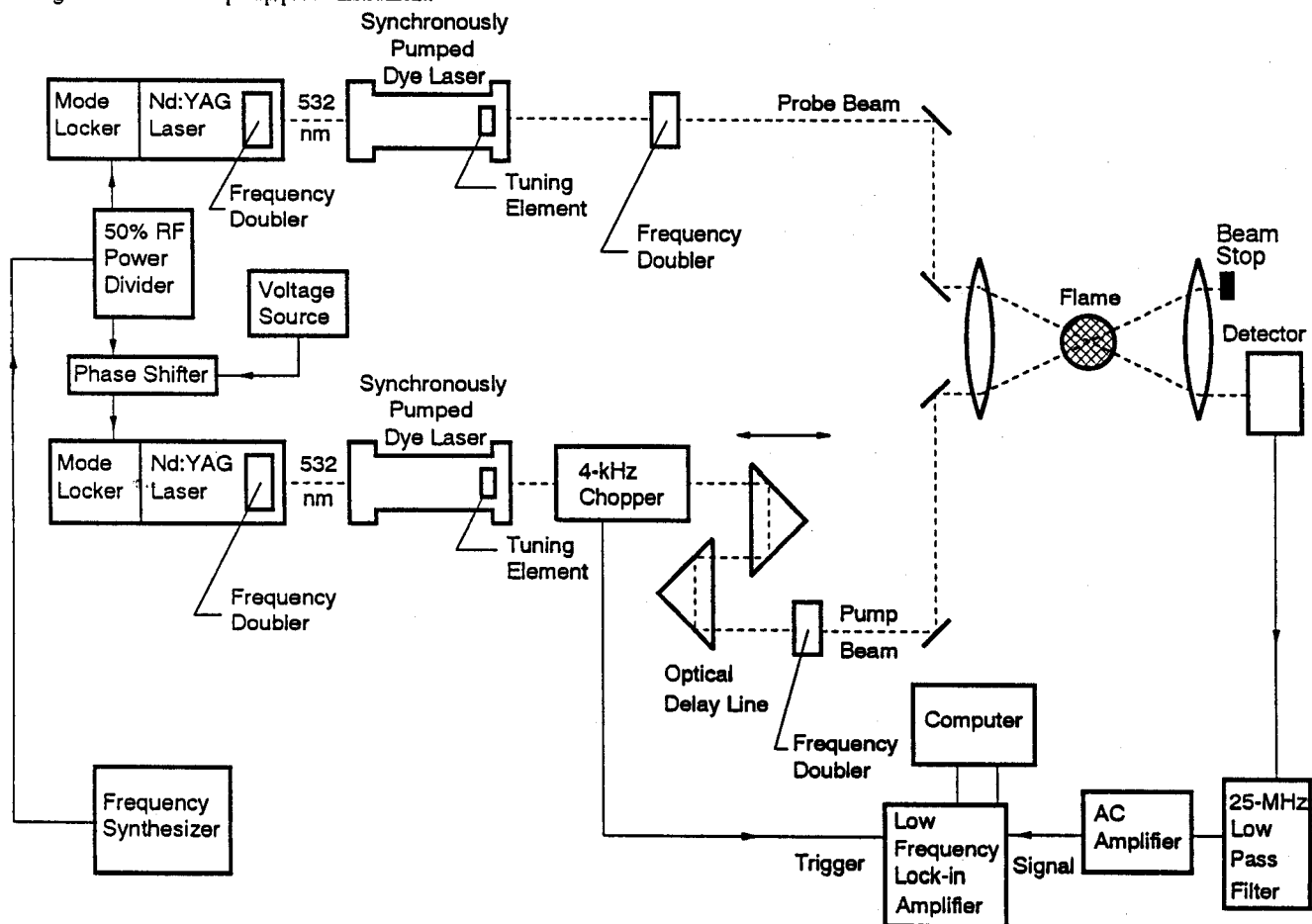


Fig. 2 Conventional pump/probe instrument using two actively mode-locked laser systems.

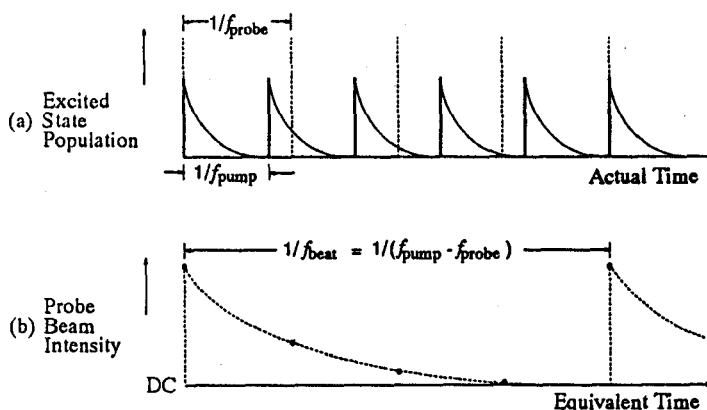


Fig. 3 ASOPS timing diagram showing (a) the excited-state population and (b) the probe beam intensity upon stimulated emission. The probe pulses in (a) are indicated by vertical dashed lines.

II. Configuration of the ASOPS Instrument

We have observed that the beat frequency should be located as far beyond the Nd:YAG power-supply noise as practical.⁷ For this reason, the ASOPS beat frequency is set at its maximum possible value. This is achieved by maximizing the mode-locking frequency of "laser A" and minimizing the mode-locking frequency of the other laser ("laser B"). The resulting frequency of ~ 160 kHz is limited by the maximum frequency of the natural acoustic resonance of the mode-locking prism for laser A, and by the maximum physical cavity length to which the end mirror of laser B can be extended. The resulting ASOPS parameters are summarized in Table I. A second benefit results from the large beat frequency: the collection time for a single decay is reduced to only 6.42 μ s, allowing approximately 100 averages within the time scale of turbulence.

Table 8.1 ASOPS operating parameters.

Repetition Rate (f_{pump}) (f_{probe})	81.640000 MHz 81.484300 MHz
Beat Frequency ($f_{\text{beat}} = f_{\text{pump}} - f_{\text{probe}}$)	155.700 kHz
Free Temporal Range ($1/f_{\text{pump}}$)	12.248898 ns
Collection Time ($1/f_{\text{beat}}$)	6.42261 μ s
Samples per Decay ($f_{\text{probe}}/f_{\text{beat}}$)	523.34

A diagram of the ASOPS instrument is shown in Fig. 4. Since the completion of the qualitative ASOPS studies,² the stainless-steel dye jets have failed due to excess wear. These have been replaced by sapphire jets, resulting in reduced high-frequency noise.⁸ A two-plate Lyot filter and an ultrafine étalon (finesse=2.2) are used for wavelength selection and bandwidth restriction. This combination is found to produce results nearly identical to those of the three-plate birefringent filter/ultrafine étalon combination that was used in previous experiments. However, the two-plate configuration is much easier to align, and produces slightly more laser power. The laser cavities of both dye lasers are positioned to produce ~ 20 ps pulses.⁷ The resulting bandwidth is at least $1.5 \times 10^{10} \text{ s}^{-1}$,^{7,9} and small enough so that the D -lines of sodium are easily resolved. The present trigger system is identical to that of our previous investigation.²

For the dual-beam ASOPS measurements, both laser A and laser B can be detected using individual EG&G FND-100Q photodiodes. The photodiode outputs can then be filtered and amplified. The resulting ASOPS signals are given by Eqs. (87) and (90) of Part 1, so that both Q and Q_{32} are measured simultaneously. This measurement would be necessary if both quantities were desired in a turbulent flame environment. However, only Q is needed in the present study. This is fortunate, since laser A produces significantly more noise than laser B,⁷ and there is only a single wideband AC amplifier in our laboratory. As seen from Eq. (90), Q can be obtained by tuning laser A to the D_2 line of sodium and detecting laser B, which is tuned to the D_1 line. Thus, the second detection system

shown in Fig. 4 is optional, and only the laser-B signal is detected in the present studies. In future studies, the simultaneous detection scheme would add little complexity to the ASOPS instrument.

The photodiode output is low-pass filtered by one of two four-pole Chebyshev filters to remove the 82-MHz modulation of the laser. Either a 20-MHz filter (Trilithic 4LM20-3-CD) or a 50-MHz filter (Texscan 4LE20-CD) can be used. When the temporal signal must be taken in the shortest time possible, the 20-MHz filter is chosen. Since the 20-MHz filter causes some slight phase distortion of the signal, the 50-MHz filter is chosen when the time to take a temporal signal is not of primary concern. For measurements of the ASOPS fundamental using a lock-in amplifier, a Texscan 4LMS-3-CD 4-pole low-pass Chebyshev filter with a 5-MHz cutoff frequency is used, since phase distortion and bandwidth reduction no longer adversely affect the signal.

The low-pass-filtered photodiode signal is then AC amplified by 1000 \times using a C-Cor 4375-A wideband AC amplifier. The amplified output is then directed to one of two detection systems, based on the type of measurement that is desired. For temporal ASOPS studies, the signal is high-pass filtered using a 5-pole 1-kHz Butterworth filter,¹⁰ and then fed to a Tektronix 602A digitizing signal analyzer. The n-pole digital Bessel filter option of this device is selected to attenuate the remaining high-frequency noise. For DC measurements, the AC amplifier output is high-pass filtered using a 7-pole 100-kHz Butterworth filter.¹⁰ The resulting signal is synchronously detected with an EG&G Princeton Applied Research 5202 high-frequency lock-in amplifier, operated with a time constant of 1 second. The DC output is directed to an analog input of a Stanford Research Systems SR510 lock-in amplifier, which is used solely as an analog-to-digital converter.

To correct for long-term drift of laser power, both lasers are monitored continuously during ASOPS experiments. Laser B is monitored using a Laser Precision Corporation Rk5100 pyroelectric radiometer, with the output directed to a second analog input of the SR510 lock-in amplifier. Laser A is chopped and then detected using an EG&G FND-100Q photodiode, the output of which is synchronously demodulated with an EG&G Princeton Applied Research 128A low-frequency lock-in amplifier with a time constant of 3 seconds. The resulting DC output is fed to a third analog input of the SR510 lock-in amplifier.

To fix the desired power of laser B before the flame, the beam is passed through a Newport 935-5 attenuator, followed by a neutral density filter. The power of laser A is selected by passing the beam through a polarization rotator/polarization beam splitter combination, followed by a neutral density filter. The beams are focused in the flame with a 200-mm focal-length lens. For the 2.9 $^\circ$ inclusive angle of the present study, the interaction length is 0.15 cm (Fig. 5 of Part 1). The resulting beam waist is used along with the present laser pulsewidth and bandwidth to calculate a saturation parameter of 2.5 mW (Part 1). For this reason, the pump and probe power are both set to 700 μ W in the flame. This value is well within the linear range of the photodetector¹¹ so that no further attenuation of laser B is necessary after the flame.

III. Calibration by Atomic Absorption Spectroscopy (AAS)

The chief objective of this study is to make quantitative concentration measurements using the ASOPS instrument. To this end, a second measurement technique, atomic absorption spectroscopy (AAS), has been implemented.

The AAS instrument is shown in Fig. 5. A tungsten filament lamp is chosen because it has been found to be an ideal light source for wavelengths in the region of the sodium D lines.¹² The lamp emission is focussed through an aperture and then chopped at 4 kHz with a PTI model OC 4000 chopper. The light is then collimated with a second lens, and directed to the same set of 200-mm lenses that are used in the ASOPS studies. The light is focussed through the center of the flame, 3.3 mm above the burner surface. The light is then collimated and passed through an aperture of < 5 mm diameter. The remaining light is then focussed into a 1/4-meter monochromator (Shoefel Instruments Model GM 252) using a 120-mm focal length lens. With entrance and exit slit-widths of less than 7 μ m, the spectral resolution of the monochromator was inadequate to fully separate the D_1 and D_2 lines. Nonetheless, the peaks are readily discerned. The monochromator is scanned using a stepper motor, with each scan being completed in 75 steps. By measuring the spectral separation of the resonance peaks, the monochromator is calibrated to a value of $1.91 \times 10^{10} \text{ s}^{-1}/\text{step}$.

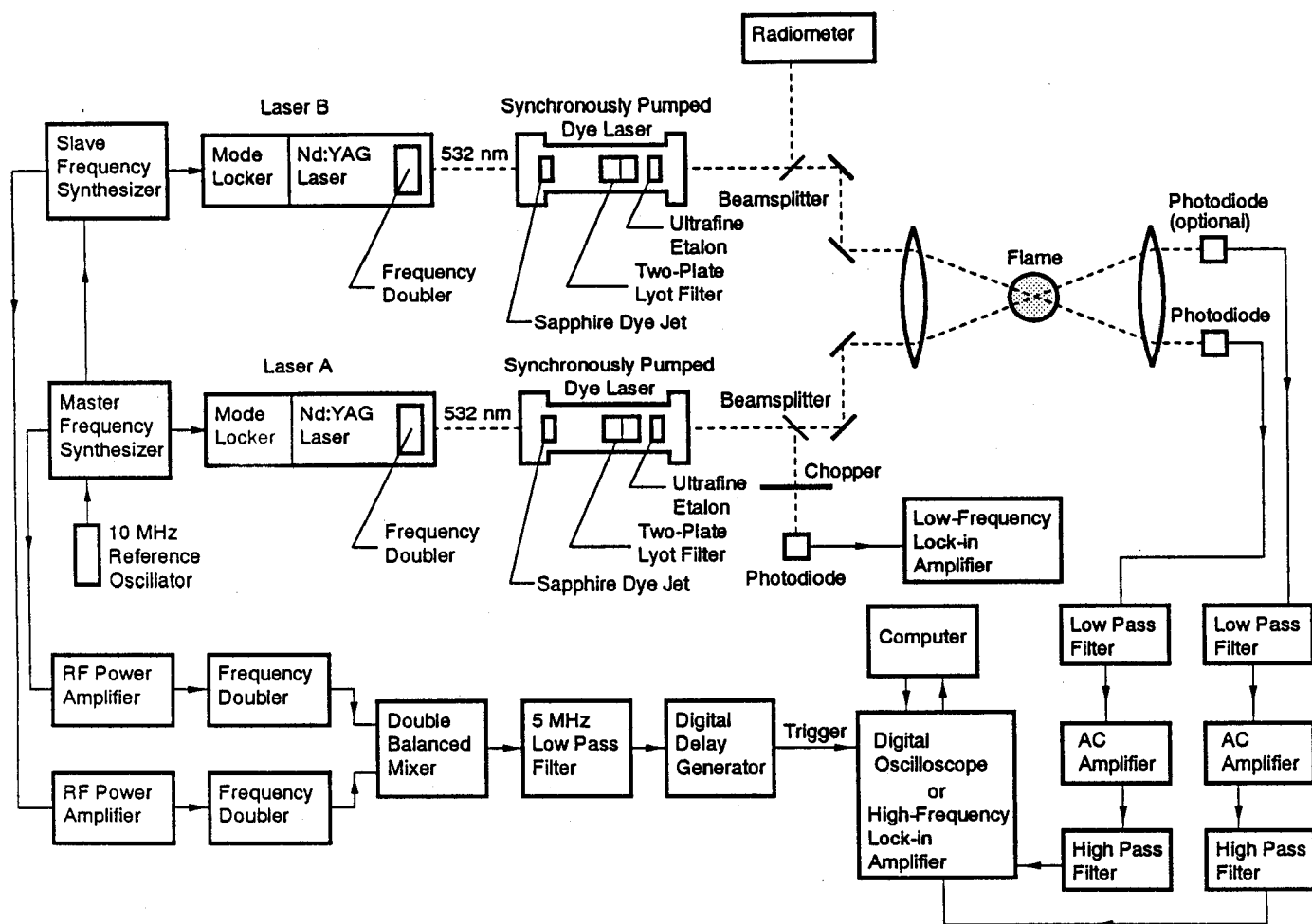


Fig. 4 ASOPS instrument diagram, including dual-beam option.

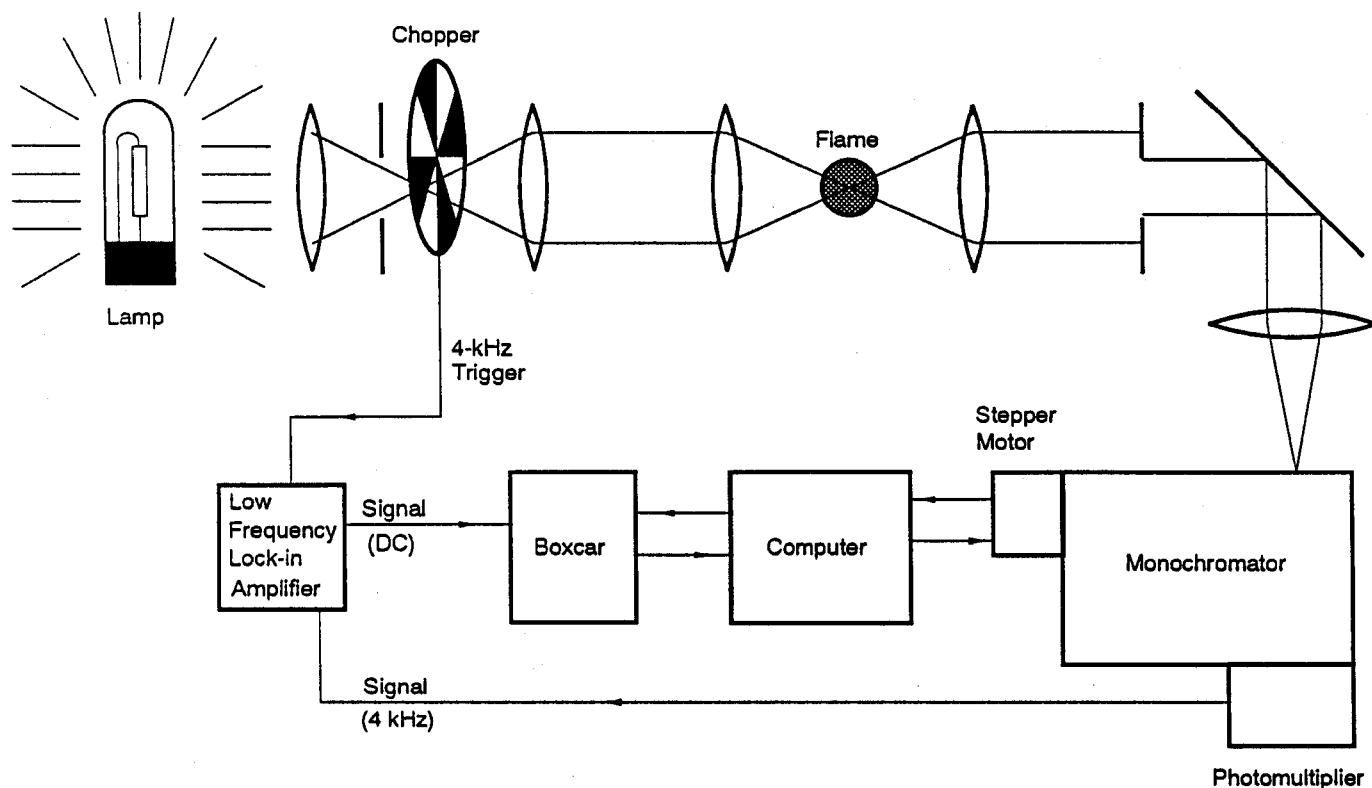


Fig. 5 AAS instrument diagram.

The light is detected using an RCA 1P28 photomultiplier, the output of which is synchronously demodulated using an EG&G Princeton Applied Research 128A low-frequency lock-in amplifier with a time constant of 300 ms. The DC lock-in output is directed to a Stanford Research Systems model SR250 gated integrator and boxcar averager, which is used solely as an analog-to-digital converter. Both the boxcar (SR245 computer interface) and the stepper motor controller are connected to a computer, so that the monochromator scanning and signal collection are synchronized. By setting the boxcar to sample the DC lock-in output at 1.43 Hz, a single scan can be taken in 53 seconds. A more detailed discussion of the stepper motor system has been given by Carter.¹³ The SNR can be enhanced by averaging over numerous scans. This is accomplished by rotating the motor to a reference position after 75 steps. Ten averages were needed for optically-thick flames, and as many as 100 averages were required for optically-thin flames. The averaged scans were analyzed using software described in detail by Carter.¹³

The premixed methane-air flame is supported by a 1-cm diameter bundle of capillary tubes (stainless steel). The bundle rests on a plastic Perkin-Elmer nebulization chamber, to which a stainless-steel pneumatic nebulizer is attached. A 1000- $\mu\text{g/ml}$ stock solution was prepared by dissolving NaCl salt in 2000 ml of deionized water. The stock solution is then diluted to make samples of lower concentration. Samples of higher concentration are prepared individually. The flow rates of CH_4 and air are 3.71 ml/s and 37.9 ml/s, respectively. Flame stability is drastically increased by adding an additional 1.54 ml/s of O_2 , resulting in an equivalence ratio of 0.78. To reduce flame fluctuations caused by room air currents, a Hastelloy X slab is placed 21 mm above the burner surface (Fig. 6).

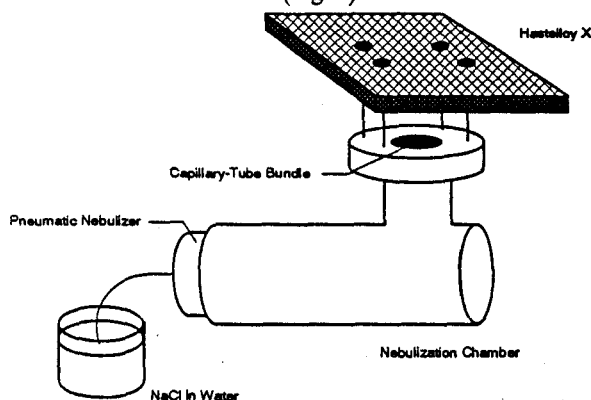


Fig. 6 Flat-flame burner and nebulizer.

The horizontal burner scan of Fig. 7 was taken using the ASOPS instrument. The variation of sodium concentration with horizontal position is accounted for by calculating an equivalent pathlength, defined by¹⁴

$$L_{\text{EQ}} = \frac{\int N_T(z) dz}{N_T(0)}, \quad (1)$$

where $N_T(0)$ is the centerline number density. Using the trapezoidal rule to calculate the integral in Eq. (1), an equivalent pathlength of 9.7 mm results.

The maximum concentration that was atomized is 10,000 $\mu\text{g/ml}$, since larger concentrations tended to clog the atomizer. The lowest concentration was 25 $\mu\text{g/ml}$, limited by the discernable change in spectral irradiance. Note that the spectral absorption is less than 1% for the 25- $\mu\text{g/ml}$ absorption scan.

The integrated absorption for small concentrations was fit using linear least squares. From the slope of the line, the atomization efficiency was found to be $\epsilon_{\text{ATOM}} = 1.7 \times 10^9 \pm 2 \times 10^6 \text{ cm}^2 (\mu\text{g/ml})^{-1}$. The standard deviation (1σ) in the integrated absorption that results from the fit is $3 \times 10^8 \text{ s}^{-1}$, represented by the error bar in the figure. The maximum solution concentration included in the least squares fit was 177 $\mu\text{g/ml}$.

Next, the largest concentrations ($>750 \mu\text{g/ml}$) were fit using a nonlinear least squares technique to determine the collisional width, $(\Delta\nu_{1/2})_C$.¹² The atomization efficiency from the optically thin curve fit was held constant. The resulting collisional linewidth is $2.7 \times 10^9 \text{ s}^{-1} \pm 3 \times 10^8 \text{ s}^{-1}$, nearly identical to the value measured by Goldsmith.¹⁵ The fit results in a standard deviation (1σ) in the integrated absorption of $1.54 \times 10^9 \text{ s}^{-1}$. Note that the reported error for the collisional linewidth is actually too small, since the atomization efficiency is also an uncertain quantity.

A flame environment has been calibrated for absolute sodium concentration using the AAS method. This calibration is used to make ASOPS measurements on a quantitative basis. An atomization efficiency of $1.7 \times 10^9 \text{ cm}^2 (\mu\text{g/ml})^{-1}$ has been measured. This can be divided by the effective pathlength of 0.97 cm to obtain a calibration factor of $1.75 \times 10^9 \text{ cm}^3 (\mu\text{g/ml})^{-1}$. Sodium chloride solution concentrations can then be converted into atomic sodium number densities in the flame. The collisional linewidth for atomic sodium has been found to be $\sim 2.7 \times 10^9 \text{ s}^{-1}$. As was shown in Part I, this width is much smaller than the spectral width of the laser, thus allowing an important simplification to the picosecond pump/probe absorption model.

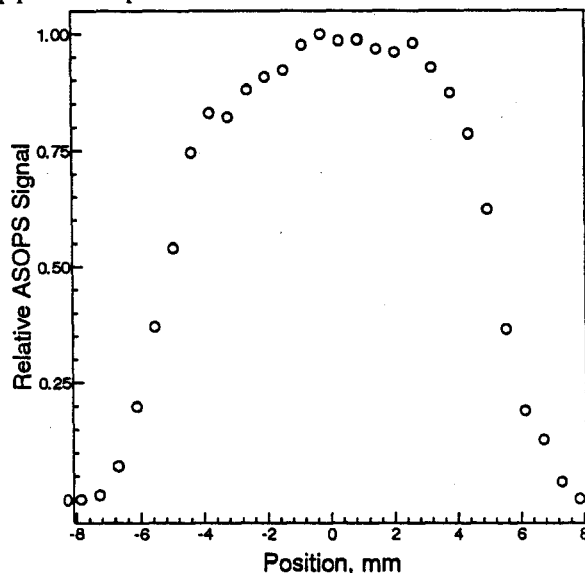


Fig. 7 Horizontal burner scan obtained using the ASOPS instrument of Fig. 4. A 100 $\mu\text{g/ml}$ solution was atomized into the flame.

IV. Experimental ASOPS Results

The present ASOPS experiments can be divided into two categories. The first ASOPS study consists of taking data while varying the sodium concentration in a flat flame burner, so that the optically-thin range can be determined. The ASOPS signal is taken using the DC measurement system with a lock-in amplifier. Once the DC study is completed, the temporal measurements are made. Data collection time is then of primary concern. The 20-MHz low-pass filter is thus used to remove as much high-frequency noise as possible. Because of the proximity of the filter's cutoff frequency to the ASOPS beat frequency, some very slight overshoot results near the peak of the signal. This is not readily observed because of the remaining high-frequency ripple, in particular, a 2-MHz rf-interference. Only 128 averages are taken for each concentration, corresponding to a potential collection time that falls within the turbulent temporal scale of $\sim 1 \text{ ms}$ or slower. For simplicity, both laser A and laser B are set to the D_2 transition at 589.00 nm, as verified using a Burleigh Wavemeter Jr. Laser B is then detected because its noise is more favorable than that of laser A.

The flat flame burner of Fig. 6 is again used. Several different sodium chloride solutions are atomized into the flame, ranging from a minimum concentration of 1 $\mu\text{g/ml}$ to a maximum concentration of 3000 $\mu\text{g/ml}$. The AAS measurements can be considered to be optically thin at or below 177 $\mu\text{g/ml}$. Both AAS and ASOPS are similar on a theoretical basis because the incident light in each case has a spectral width that is large compared to the linewidth of the individual sodium D lines. Thus the optically thin regime for ASOPS should also end at or below approximately 177 $\mu\text{g/ml}$.

However, the effective ASOPS interaction length is only 0.15 cm for the present geometry. By placing the center of the interaction volume approximately 3 mm past the burner center, the pump and probe beams must traverse much of the flame before they are crossed. The resulting pump and probe irradiance at the crossing volume will be greatly attenuated when optically-thick conditions are present. Consequently, the ASOPS signal should drop. Since the AAS signal continues to increase as the sodium concentration surpasses 177 $\mu\text{g/ml}$, the ASOPS method should serve as a much better indicator of the onset of nonlinear conditions. This might not be true if the crossing volume had been positioned near the front edge of the flame.

The ASOPS results obtained using a lock-in amplifier are shown in Figs. 8 and 9. In Fig. 8, the linear regime is shown to end between a concentration of 100 $\mu\text{g/ml}$ and 177 $\mu\text{g/ml}$. This is a somewhat lower concentration than that predicted by the AAS study. Since the ASOPS method is more sensitive to the onset of optically thick conditions, this result is not surprising. Moreover, the average ASOPS values clearly result in less scatter from linearity than the AAS data points. This is demonstrated by the superimposed linear least squares fit, which results in a standard deviation (1σ) of only 1.0% of the maximum signal. This deviation is represented by the error bar of Fig. 8. The actual fluctuation of the experimental data is much larger, as shown by the error bars in Fig. 9. These represent the sample standard deviation of each point; each point is the average of 3 to 5 individual samples. Nearly all of the observed deviation is caused by long-term drift in the wavelength of the lasers.

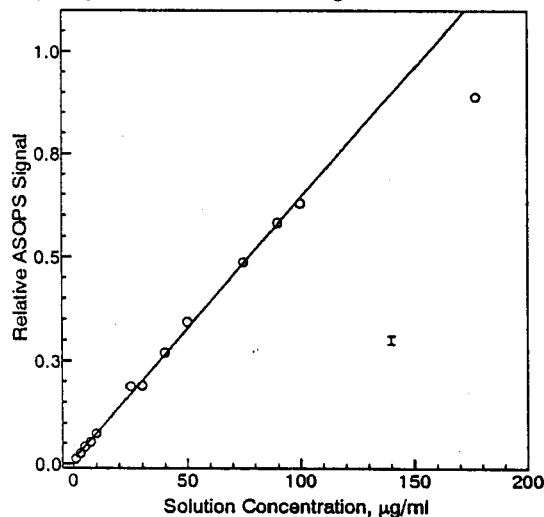


Fig. 8 Variation of the ASOPS signal with atomized solution concentration. The line is a linear least-squares fit to those points having a concentration less than or equal to 100 $\mu\text{g/ml}$. The point at 177 $\mu\text{g/ml}$ is plotted to emphasize the departure from linearity. The error bar represents the standard deviation (1σ) of the data from the line. The actual deviation for each point is much larger, as shown in Fig. 9.

The lowest concentration that is detected is 1 $\mu\text{g/ml}$. Using a lock-in amplifier, smaller concentrations can ideally be detected, since at this concentration the SNR is above unity. Each data point is taken by averaging the lock-in amplifier output for 10 seconds. For a concentration of 1 $\mu\text{g/ml}$, the resulting standard deviation is typically only 19% of the average signal magnitude. Unfortunately, a sizeable residual buildup of sodium chloride in the nebulizer causes a background signal. This signal tends to drift with time. To account for the resulting bias, deionized water is periodically fed to the nebulizer, and the resulting signal is then recorded. This signal is then subtracted from the data in software. The magnitude of the residual background signal is typically 26% of the uncorrected signal magnitude for the 1 $\mu\text{g/ml}$ solution.

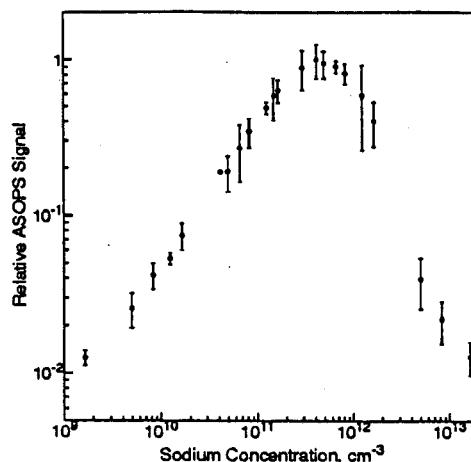


Fig. 9 Variation of the ASOPS signal with sodium number density, calculated from the AAS calibration parameter. Each point is an average of several points, ranging from three to five values. For this reason, the error bars represent the sample standard deviation (1σ).

Knowing the extent of the linear range, the experimental emphasis was shifted to temporal studies. An ASOPS signal obtained with 128 averages for a 100 $\mu\text{g/ml}$ solution is shown in Fig. 10. The Tektronix 602A digital oscilloscope is operated in the real-time acquisition mode. The resulting peak SNR is approximately 10:1. The 1:1 SNR point is found to occur at $\sim 3 \mu\text{g/ml}$, as shown in Fig. 11. This detection limit results largely from the 2-MHz rf interference.⁷ The AC amplifier is set to increase the signal by a factor of 1000. This means that the actual photodiode output signal is only $\sim 5 \mu\text{V}$. Multiplying the solution concentration by the AAS calibration factor, the sodium number density is found to be $5.3 \times 10^9 \text{ cm}^{-3}$. In Part 1, a detection limit for OH is estimated by assuming a 10^{-8} depth of modulation. The present minimum modulation depth is clearly not this small. However, the ratio between the OH and Na estimates will remain unchanged, no matter what the assumed value of the modulation depth may happen to be. Multiplying the present Na number density by this ratio (3.8×10^7), a detection limit of $2 \times 10^{17} \text{ cm}^{-3}$ is estimated for the hydroxyl radical. This calculation assumes that the $Q_1(9)$ line of $A^2\Sigma^+(v'=0) \rightarrow X^2\Pi^+(v''=0)$ OH is detected in a flame at 2000 K. Recall from Part 1 that this calculation assumes 1 mW of pump and probe power for both OH and Na. For sodium, this value is chosen to preclude saturation. In the case of hydroxyl, the saturation parameter increases to 900 mW. The 1-mW value is chosen in the present calculation because it is a conservative estimate of the available UV laser power.⁸ Any future improvements in laser technology that result in a substantial increase in UV laser power will thus improve the detection limit for OH.

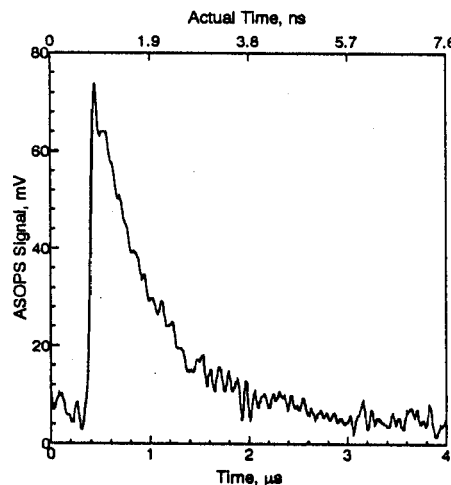


Fig. 10 ASOPS decay obtained with only 128 averages. A 100 $\mu\text{g/ml}$ solution was atomized into the flame.

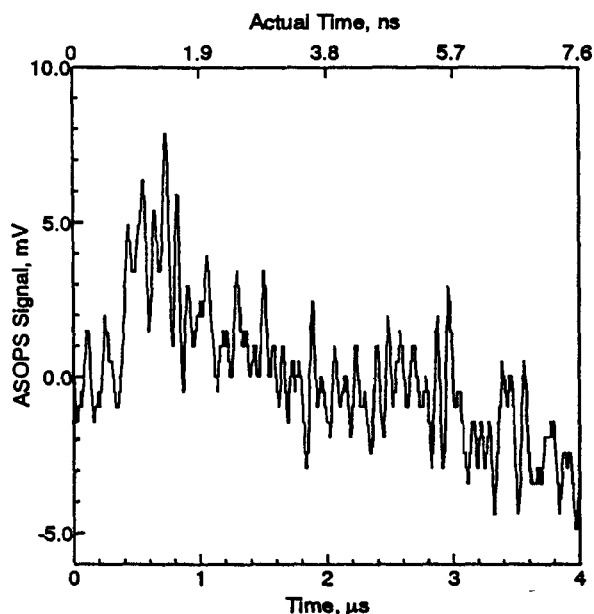


Fig. 11 ASOPS decay obtained with only 128 averages. A 3 $\mu\text{g/ml}$ solution was atomized into the flame. The signal is obscured by 2-MHz rf interference and by 62-kHz Nd:YAG laser noise.⁷

The effects of additional signal averaging are demonstrated for the 100- $\mu\text{g/ml}$ solution in Fig. 12. Here, 1024 averages are taken. The resulting peak SNR is now $\sim 40:1$, limited by the quantizer resolution of the digital oscilloscope. However, the SNR is not substantially improved with 1024 averages for the case of the 3 $\mu\text{g/ml}$ solution. This is demonstrated in Fig. 13, where the quantizer resolution is shown to limit the peak SNR to $\sim 4:1$.

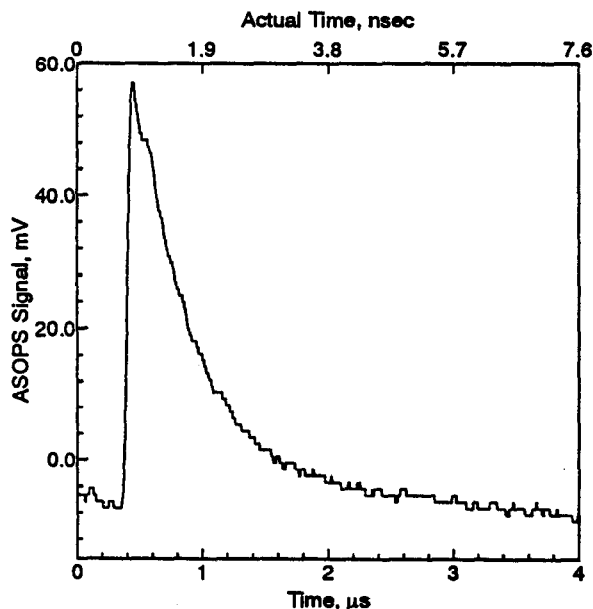


Fig. 12 ASOPS decay obtained with 1024 averages. A 100 $\mu\text{g/ml}$ solution was atomized into the flame. The slight distortion at the peak of the signal is caused by the 20-MHz low-pass filter.

The present lean CH_4/air flame is chosen because the products of combustion are mainly CO_2 , H_2O vapor and air. Ignoring the effects of temperature gradients, the resulting quenching rate coefficient should be similar at the burner center and the burner edge, because entrainment of room air should not significantly alter the overall flame composition. Because the temperature is likely to be larger at the center of the burner, the corresponding value of Q should be slightly smaller at the burner edge.⁷

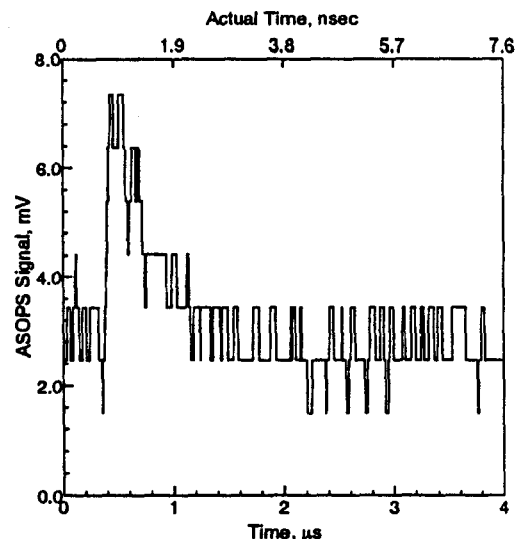


Fig. 13 ASOPS decay obtained with 1024 averages. A 3 $\mu\text{g/ml}$ solution was atomized into the flame. Much of the noise remains, and the effects of quantizer resolution are evident.

To simplify the measurement of Q , the dual-beam ASOPS excitation method is selected. The 50-MHz low-pass filter is chosen to minimize distortion, and 8192 averages are taken. This amount of averaging is not necessary to obtain a decay—the large amount is taken to ensure a reliable estimate of Q . The 100- $\mu\text{g/ml}$ NaCl solution is used. Two points are taken: one at the burner center and one 4 mm from the burner center. The resulting $3P$ lifetimes are 950 ps and 780 ps, respectively. This range is in excellent agreement with the value of 830 ps measured by Fourkas *et al.*^{16,17} using a picosecond transient induced grating method. As expected, the variation is quite small (18%). For this reason, the ASOPS flame profile of Fig. 7 is not corrected for quenching. The resulting error in the effective absorption pathlength is smaller than the deviation of the AAS results due to other problems such as fluctuations in atomizer efficiency. The signal magnitude at 4 mm is small enough that the coherent laser noise becomes a limiting factor, as shown in Fig. 14. To obviate the effects, a linearly increasing value is subtracted from the signal for times ranging from $t=0$ to $t=2$ μs . This line is calculated by taking the average of the signal for $t < 0$. The average value is assumed to hold at $t=0$. A line is drawn to intersect a point on the signal at $t=2$ μs . This line is then subtracted from the signal over the same temporal range. The resulting curve is shown by the open circles in Fig. 15. The solid curve is the exponential fit for Q , obtained using a nonlinear least squares technique.

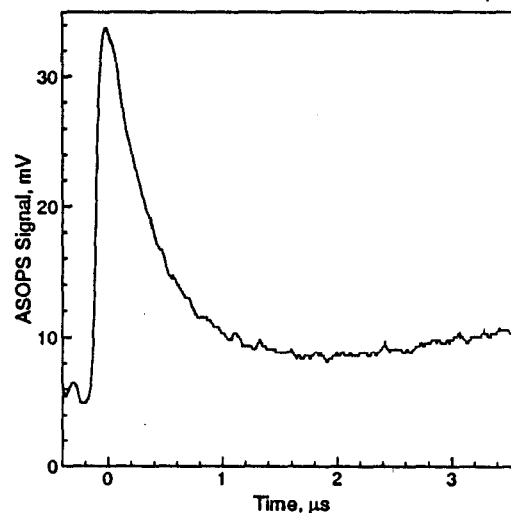


Fig. 14 ASOPS signal obtained 4 mm from the center of the laminar flat-flame burner. The signal rests on noise from the Nd:YAG laser power supply,⁷ which remains even though 8192 averages were taken.

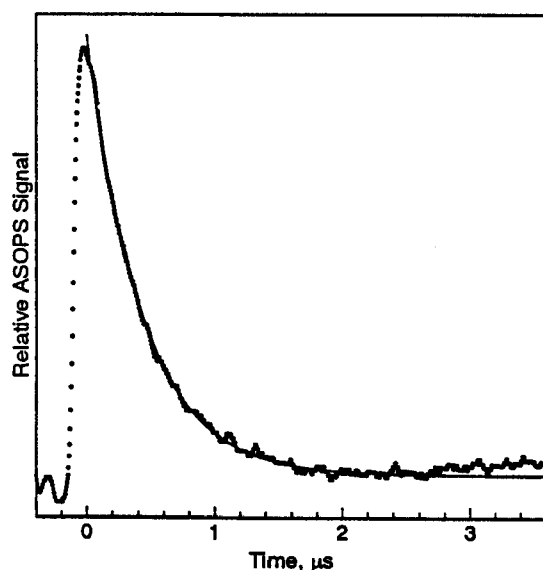


Fig. 15 An exponential fit (solid curve) to the data of Fig. 8.9 (open circles) using a non-linear least squares technique.⁷ The resulting lifetime becomes 780 ps, corresponding to a quenching rate coefficient of $Q=1.22 \times 10^9 \text{ s}^{-1}$.

V. Summary

The first quantitative evaluation of the ASOPS technique in a flame environment has been demonstrated. ASOPS data are taken in a time scale adequate for many turbulence applications, while at the same time yielding an impressive SNR under optically-thin conditions. A qualitative prediction of the eventual detection limit for the $Q_1(9)$ line of $A^2\Sigma^+(v'=0) \rightarrow X^2\Pi^+(v''=0)$ OH yields a number density of $2 \times 10^{17} \text{ cm}^{-3}$. Although this quantity is approximately two orders of magnitude too large for practical flame studies, an increase in laser power of two orders of magnitude would drop the detection limit by the required factor of 100. The detection limit for the ASOPS technique is not governed by shot noise. Instead, deterministic noise in the detection electronics dominates the SNR. Thus if both the pump and probe power are increased by a factor of 100, the detection limit should increase by four orders of magnitude for ASOPS.

The dual-beam ASOPS excitation method has been demonstrated for the first time. It is shown that Q can be obtained in a single measurement using this configuration. The range of values of Q that we measured is in excellent agreement with that reported in the literature.

Finally, we note that the lasers in our experiments had many undesirable characteristics compared to technology that is commercially available. New mode-locked laser systems based on Ti:sapphire technology produce two orders of magnitude more average power. Kafka *et al.*¹⁸ operated two of these lasers in the ASOPS configuration, obtaining an impressive cross-correlation of 150 fs. This compares to a value of 7 ps for our lasers.¹⁹ The Ti:sapphire lasersystem produced pulses of width that was selectable from 40 fs to 100 ps, with average output power over 3.5 W for the entire range of pulsewidths (and a wavelength of 780 nm).²⁰ Although we are not aware of any noise comparisons between mode-locked Ti:sapphire lasers and mode-locked Nd:YAG lasers, the noise from a mode-locked Ti:sapphire laser has been found to be favorable when compared to that from a colliding-pulse mode-locked dye laser.²¹

Acknowledgments

The authors wish to thank Professor Fred Lytle, Department of Chemistry, Purdue University, for the loan of much of the equipment for the present study. This work was sponsored by the U.S. Air Force Office of Scientific Research, Air Force Systems Command, under grant AFOSR-84-0323.

References

1. B. D. Thompson, M.S. Thesis, (Purdue University, W. Lafayette, IN, 1992); N. H. Wrobel and N. H. Pratt, in *Seventeenth Symposium (International) on Combustion*, The Combustion Institute, Pittsburgh, PA, 1978, pp. 957-966.
2. G. J. Fiechtner, G. B. King, N. M. Laurendeau and F. E. Lytle, *Appl. Opt.* **31**, 2849-2864 (1992).
3. R. J. Kneisler, F. E. Lytle, G. J. Fiechtner, Y. Jiang, G. B. King and N. M. Laurendeau, *Opt. Lett.* **14**, 260-262 (1990).
4. R. A. Beaman, Ph.D. dissertation, (University of Wales, 1985); A. J. Langley, R. A. Beaman, J. Baran, A. N. Davies, W. J. Jones, *Opt. Lett.* **10**, 327-329 (1985); A. J. Langley, R. A. Beaman, A. N. Davies, W. J. Jones and J. Baran, *Chem. Phys.* **101**, 117-125 (1986); R. A. Beaman, A. N. Davies, A. J. Langley, W. J. Jones and J. Baran, *Chem. Phys.* **101**, 127-132 (1986); W. J. Jones, *J. Chem. Soc., Faraday Trans. 2* **83**, 693-705 (1987); W. Mallawaarachchi, A. N. Davies, R. A. Beaman, A. J. Langley, W. J. Jones, *J. Chem. Soc. Faraday Trans. 2* **83**, 707-722 (1987).
5. B. A. Mann, Ph.D. dissertation, (University of Reading, Whiteknights, Reading, Berks, England, 1991).
6. G. J. Fiechtner, G. B. King, N. M. Laurendeau, R. J. Kneisler and F. E. Lytle, *Appl. Spectrosc.* **43**, 1286-1287 (1989).
7. G. J. Fiechtner, Ph.D. dissertation (Purdue University, West Lafayette, Indiana, 1992).
8. H. P. H rri, S. Leutwyler and E. Schumacher, *Rev. Sci. Instrum.* **53**, 1855 (1982).
9. G. J. Blanchard and M. J. Wirth, *Opt. Commun.* **53**, 394-400 (1985).
10. A. I. Zverev, *Handbook of Filter Synthesis*, John Wiley and Sons, New York, NY, 1967.
11. P. A. Elzinga, M.S. thesis, (Purdue University, West Lafayette, Indiana, 1986).
12. C. Th. J. Alkemade, Tj. Hollander, W. Snelleman and P. J. Th. Zeegers, *Metal Vapours in Flames*, Pergamon Press, New York, NY (1982).
13. C. D. Carter, Ph.D. dissertation, (Purdue University, West Lafayette, Indiana, 1990).
14. R. P. Lucht, D. W. Sweeney, and N. M. Laurendeau, *Combust. Sci. and Tech.* **42**, 259 (1985).
15. J. E. M. Goldsmith, *Opt. Lett.* **6**, 525-527 (1981).
16. J. T. Fourkas, T. R. Brewer, H. Kim and M. D. Fayer, *Opt. Lett.* **16**, 177-179 (1991).
17. R. P. Lucht, R. Trebino and L. A. Rahn, Sandia report SAND91-8556, Sandia National Laboratories, Livermore, CA, 1991.
18. J. D. Kafka, J. W. Pieterse and M. L. Watts, *Opt. Lett.* **17**, 1286-1288 (1992).
19. P. A. Elzinga, R. J. Kneisler, F. E. Lytle, Y. Jiang, G. B. King and N. M. Laurendeau, *Appl. Opt.* **26**, 4303 (1987); R. J. Kneisler, F. E. Lytle, G. J. Fiechtner, Y. Jiang, G. B. King and N. M. Laurendeau, *Opt. Lett.* **14**, 260 (1989).
20. J. D. Kafka, M. L. Watts and J. W. Pieterse, *IEEE J. Quantum Electron.* **QE-28**, 2151-2162 (1992).
21. J. Son, J. V. Rudd and F. Whitaker, *Opt. Lett.* **17**, 733-735 (1992).

Morning session 5A: Waste Incineration; Chair: Brian Higgins, University of California at Berkeley

- 8:40 92-63 Time Resolved Measurements of Two-Dimensional Temperature Fields in an Acoustically Excited Dump Combustor, C. Cadou, J. Willis, A. R. Karagozian, Department of Mechanical, Aerospace, & Nuclear Engineering, R. Marchant and O. I. Smith, Department of Chemical Engineering, University of California at Los Angeles, Los Angeles, CA.
- 9:00 92-64 Destruction of Toxic Compounds in Combustion Augmented by a Radio Frequency Induction Plasma, S. A. Engleman, R. F. Sawyer, University of California at Berkeley, Berkeley, CA, A. Odeide, and D. Lucas, Lawrence Berkeley Laboratory, Berkeley, CA.
- 9:20 92-65 In-situ, Real-time Measurement of Chlorinated Hydrocarbon Concentrations in Combustion Systems, C. S. McEnally and R. F. Sawyer, Department of Mechanical Engineering, University of California at Berkeley, Berkeley, CA, C. P. Koshland, Department of Environmental Health Sciences, University of California at Berkeley, Berkeley, CA and D. Lucas, Energy and Environment Division, Lawrence Berkeley Laboratory, Berkeley, CA.
- 9:40 92-66 Mechanisms of Phosgene Formation, M. J. Thomson and B. S. Higgins, Mechanical Engineering, University of California at Berkeley, Berkeley, CA, D. Lucas, Energy and Environment Division, Lawrence Berkeley Laboratory, Berkeley, CA, C. P. Koshland, Department of Environmental Health Sciences, University of California at Berkeley, Berkeley, CA, and R. F. Sawyer, Department of Mechanical Engineering, University of California at Berkeley, Berkeley, CA.
- 10:00 92-67 High Temperature UV-Visible Absorption Spectrum Measurements and Estimated Primary Photodissociation Rates of Formaldehyde, 1-Chlorobenzene & 1-Chloronaphthalene, M. W. Mackey, J. W. Daily, Center for Combustion Research, University of Colorado at Boulder, Boulder, CO and J. T. McKinnon, Colorado School of Mines, Golden, CO.
- 10:20 Break

Morning session 6A: Diagnostics; Chair: David Warren, Brigham Young University

- 10:40 92-68 Picosecond Pump/Probe Absorption Spectroscopy for Quantitative Concentration Measurements in Turbulent, High-Pressure Flames, G. J. Fiechtner, Department of Mechanical Engineering, University of Colorado, Boulder, CO, G. B. King and N. M. Laurendeau, School of Mechanical Engineering, Purdue University, West Lafayette, IN.
- 11:00 92-69 Amplified Spontaneous Emission Measurements of Atomic Oxygen in Low-Pressure Flames, M. S. Brown, F. S. Long, and J. B. Jeffries, Molecular Physics Laboratory, SRI International, Menlo Park, CA.
- 11:20 92-70 Soot Formation in Turbulent Flames, E. Gutmark, T. P. Parr, D. M. Hanson-Parr, and K. C. Schadow, Research Department, Naval Air Warfare Center Weapons Division, China Lake, CA.
- 11:40 92-71 Calculated Transition Probabilities in the A-X System of OH, J. Luque, and D. R. Crosley, Molecular Physics Laboratory, SRI International, Menlo Park, CA.
- 12:00 92-72 Real-Time Optical Diagnostics for the Basic Oxygen Steelmaking Process, D. K. Ottesen, R. H. Hurt, and D. R. Hardesty, Combustion Research Facility, Sandia National Laboratories, Livermore, CA.

Morning session 5B: Gravitational Effects; Chair: Corey Dunskey, Sandia National Laboratories

- 8:40 92-100 Reduced-Gravity Observations of Near-Transition Gas Jet Diffusion Flames, L. Zhou, University of California at Berkeley, Berkeley, CA, D. F. Vaughan, Baldwin-Wallace College, Berea, OH, D. P. Stocker, NASA Lewis Research Center, Cleveland, OH, U. Hegde, Sverdrup Technology, Inc., Brookpark, OH and M. Y. Bahadori, Science Applications International Corporation, Torrance, CA.
- 9:00 92-101 Numerical and Experimental Investigation of the Effects of Buoyancy on Laminar Diffusion Flames, M. Y. Bahadori, Science Applications International Corporation, Torrance, CA, R. B. Edelman, Rockwell International Corporation, Canoga Park, CA, and D. P. Stocker, NASA Lewis Research Center, Cleveland, OH.
- 9:20 92-102 An Analytical Model for Gravitational Effects on Burke-Schumann Flames, U. Hegde, Sverdrup Technology, Inc., Cleveland, OH and M. Yousef Bahadori, Science Applications International Corporation, Torrance, CA.
- 9:40 92-103 The Effects of Gravity on Wrinkled Laminar Flames, L. W. Kostiuk, L. Zhou, and R. K. Cheng, Combustion Group, Lawrence Berkeley Laboratory, Berkeley, CA.
- 10:00 92-104 Experimental Observations of the Effect of Gravity Changes on Smoldering Combustion, J. L. Torero, A. C. Fernandez-Pello, Department of Mechanical Engineering, University of California at Berkeley, Berkeley, CA, D. Urban, Sverdrup Technology, Inc., Brookpark, OH.
- 10:20 Break

Morning session 6B: Flame Spread and Laminar Flames; Chair: John Card, University of California at San Diego

- 10:40 92-105 Liquid-Phase Flow and Temperature Field Measurements of Flame Spread over Laboratory-Scale Alcohol Pools, F. J. Miller and H. D. Ross, NASA Lewis Research Center, Cleveland, OH.
- 11:00 92-106 Investigation of Controlling Parameters in Transition Between Thermally Thin and Thermally Thick Flame Spread Over Solid Fuels in an Opposing Flow, J. West, Subrata Bhattacharjee, Department of Mechanical Engineering, San Diego State University, San Diego, CA, and R. A. Altenkirch, Department of Mechanical and Nuclear Engineering, Mississippi State University, Mississippi State, MS.
- 11:20 92-107 The Role of Kinetic, Transport, and Thermodynamic Properties on Flame Spread Over a Thin Solid Fuel in an Opposed-Flow Environment, S. Bhattacharjee, D. Seaton, Department of Mechanical Engineering, San Diego State University, San Diego, CA, and R. A. Altenkirch, Department of Mechanical and Nuclear Engineering, Mississippi State University, Mississippi State, MS.
- 11:40 92-108 Laminar Burning Velocities and Markstein Numbers of Hydrocarbon/Air Flames, L.-K. Tseng, Department of Aerospace Engineering, The University of Michigan, Ann Arbor, MI, M. A. Ismail, Department of Mechanical Engineering, Helwan University, Cairo, Egypt, and G. M. Faeth, Department of Aerospace Engineering, The University of Michigan, Ann Arbor, MI.
- 12:00 92-109 The Effect of Wall Temperature on Stagnation and Sidewall Flame Quenching and the Resulting Heat Transfer, L. G. Connelly III, R. Greif and R. F. Sawyer, Department of Mechanical Engineering, University of California at Berkeley, Berkeley CA.